Dynamic Stability, Blowoff, and Flame Characteristics of Oxy-Fuel Combustion

by

Andrew Philip Shroll

B.S., Mechanical Engineering
University of Nebraska-Lincoln (2008)

Submitted to the Department of Mechanical Engineering
in partial fulfillment of the requirements for the degree of

Master of Science in Mechanical Engineering

at the

MASSACHUSETTS INSTITUTE OF TECHNOLOGY

June 2011

Author .....
Department of Mechanical Engineering
May 6, 2011

Certified by .....
Ahmed F. Ghoniem
Ronald C. Crane ('72) Professor
Thesis Supervisor

Accepted by .....
David Hardt, Professor of Mechanical Engineering
Chairman, Department Committee on Graduate Theses

Dynamic Stability, Blowoff, and Flame Characteristics of Oxy-Fuel Combustion

by

Andrew Philip Shroll

Submitted to the Department of Mechanical Engineering
on May 6, 2011, in partial fulfillment of the
requirements for the degree of
Master of Science in Mechanical Engineering

Abstract

Oxy-fuel combustion is a promising technology to implement carbon capture and sequestration for energy conversion to electricity in power plants that burn fossil fuels. In oxy-fuel combustion, air separation is used to burn fuel in oxygen to easily obtain a pure stream of carbon dioxide from the products of combustion. A diluent, typically carbon dioxide, is recycled from the exhaust to mitigate temperature. This substitution of carbon dioxide with the nitrogen in air alters the thermodynamics, transport properties, and relative importance of chemical pathways of the reacting mixture, impacting the flame temperature and stability of the combustion process.

In this thesis, methane oxy-combustion flames are studied for relevance to natural gas. First, a numerical 1-D strained flame shows significantly reduced consumption speeds for oxy-combustion compared to air combustion at the same adiabatic flame temperature. Competition for the H radical from the presence of carbon dioxide causes high CO emissions. Elevated strain rates also cause incomplete combustion in oxy-combustion, demonstrated by the effect of Lewis number with a value greater than one for flame temperatures under 1900 K.

Most of this work focuses on experimental results from premixed flames in a 50 kW axi-symmetric swirl-stabilized combustor. Combustion instabilities, upon which much effort is expended to avoid in gas turbines with low pollutant emissions, are described as a baseline for the given combustor geometry using overall sound pressure level maps and chemiluminescence images of 1/4, 3/4, and 5/4 wave mode limit cycles. These oxy-combustion results are compared to conventional air combustion, and the collapse of mode transitions with temperature for a given Reynolds number is found. Hysteresis effects in mode transition are important and similar for air and oxy-combustion.

Blowoff trends are also analyzed. While oxy-combustion flames blow off at a higher temperature for a given Reynolds number due to weaker flames, there is an unexpected negative slope in blowoff velocity vs temperature for both air and oxy-combustion. The blowoff data are shown to collapse due to blowoff velocity being inversely proportional to the molar heat capacities of the burned gas mixtures at a

given power. Finally, particle image velocimetry results are discussed to relate flow structures to corresponding flame structures.

Thesis Supervisor: Ahmed F. Ghoniem
Title: Ronald C. Crane ('72) Professor

Acknowledgments

I would like to thank Professor Ghoniem first and foremost for his guidance and insight on this project. His expertise and breadth of knowledge have inspired me in energy and combustion research. I also could not have made it without the help, direction, and many lessons from Santosh Shanbhogue. He has been critical to my progress as a student and researcher. The flame code and experimental setup of this thesis build off of previous work by Ray Speth, and I am grateful for his patience in imparting a sliver of his expertise to me. I owe much to the rest of the Reacting Gas Dynamics Lab as well for answering my many questions. It has been a pleasure working with everyone.

The help and support of my classmates and friends have been indispensable in my time at MIT. I am truly thankful for the friends I have from all the places I have lived. To my many teachers and mentors from MIT and UNL, as well as those outside academia, I thank them for their generosity and for developing a drive in me to make a difference. Most of all, I appreciate the love and support of my family. They have been with me every step of the way.

This work has been sponsored by King Abdullah University of Science and Technology (KAUST), Grant number KSU-I1-010-01.

Contents

List of Figures

List of Tables

Chapter 1

Introduction

Energy in valuable forms is an essential part of modern life. World-wide energy consumption continues to rise as a result of growing population and increased development in many countries. Currently, 85% of this energy is obtained from fossil resources, and there is an appreciable risk of anthropogenic climate change by continued release of carbon dioxide into the atmosphere through combustion of these fuels [10]. One strategy to reduce the net amount of CO_2 released is to sequester (pump into the earth) the CO_2 produced at power plants that convert the chemical energy in fossil fuels into electricity. Oxy-fuel combustion, on which this thesis focuses, is one of the viable methods to capture carbon dioxide for sequestration. Carbon capture and sequestration (CCS) to prevent and/or alleviate anthropogenic climate change is thus the motivation for this work. More specifically, this thesis focuses on oxy-fuel combustion as applied to the field of combustion dynamics.

1.1 Oxy-Fuel Combustion for Carbon Capture

There are currently three major avenues toward CCS. The first is post-combustion capture, in which CO_2 is separated from flue gasses in a traditional power plant. This is generally accomplished with monoethanolamine absorption cycles. The second avenue is pre-combustion capture, where a scheme such as an integrated gasification combined cycle (IGCC) is used to produce synthesis gases which are burned in a way

that facilitates CCS. While pre-combustion capture could be used with natural gas via fuel reforming, the most promising route for pre-combustion capture is coal with IGCC because of the advantages IGCC provides in cleaning up a dirty fuel like coal. There are also other advanced capture schemes such as chemical looping currently being researched.

The third major avenue for CCS, oxy-fuel combustion (also written as oxy- combustion), is in itself not a new technology. The traditional meaning of oxy-fuel combustion is to burn a fuel in pure oxygen rather than in air, which contains only 21% oxygen by volume. Burning in pure oxygen allows for much higher flame temperatures because the inert nitrogen in air is no longer present as a heat sink. Common uses under this meaning include oxy-acetylene welding and heating of glass furnaces.

Oxy-fuel combustion as applied to CCS, however, requires lower flame temperatures to stay within the material limits in power plants. This implies that some diluent besides nitrogen must be used. The principle of oxy-combustion for CCS is burning fuel in a mixture of oxygen and a diluent that is recycled from the flue gas. Since the products of combustion are carbon dioxide and water, one of these two is used. The products (flue gas) are then comprised (ideally) of only CO_2 and H_2O. The water is then condensed, providing a pure stream of CO_2 for sequestration. Carbon dioxide is currently being studied the most as the diluent of choice, but Richards et al. [28] have put significant effort into H_2O dilution.

Oxy-combustion is generally associated with coal because it is a more likely target for CCS: a coal power plant produces about three times as much CO_2 per unit of electric energy as a natural gas combined cycle (NGCC) power plant. However, natural gas power plants should also be considered for oxy-combustion because, for example, about 19% of electricity generation in the U.S. is from natural gas [8]. In addition, the substantial increase in natural gas reserves from shale gas technology in recent years suggests there will be significant growth, especially in North America, in the amount of electricity produced from natural gas.

Each of the types of carbon capture includes an energy penalty, and in oxy-fuel combustion the main penalty is in separating the oxygen out of air. Energy is also

needed to pump CO_2 into the ground for sequestration or an application such as enhanced oil recovery (EOR). The most common industrial scale air separation method is cryogenic distillation. Kvamsdal et al. [18] showed that the efficiency penalty of CCS for NGCC with cryogenic separation is about on par with post-combustion capture. Oxy-combustion shows a clear advantage in efficiency, however, when coupled with an advanced separation method such as an ion transport membrane (ITM).

While excellent retrofit potential is claimed for oxy-combustion of natural gas in boiler systems [32], there are challenges in retrofitting existing gas turbines for oxy-combustion. Although existing compressors and turbines could be used, a gas turbine designed for the new working fluid (mostly CO_2) would be required to avoid a drop in performance [6, 15].

1.2 Oxy-Fuel Combustion Dynamics

The premixed mode of combustion is susceptible to instabilities, which are a feedback process between combustion, heat release, and the acoustic field. There have been a number of reviews on this topic [22, 14] that detail various mechanisms leading to instability and control strategies. However, there is a need for further studies to understand several remaining questions regarding, for example, mode transitions (how the flow/combustion characteristics couple with a particular mode or its harmonics during any change in operating conditions such as loading, reactants, temperature and fuel characteristics).

In general, the transition in the stability characteristics of the combustor, from stable to unstable or from one mode to its harmonics, can be lumped into two categories. The first kind of transition occurs when the flame-stabilization mechanism changes for a small change in conditions, such as from a wake mode to a shear layer mode and vice-versa [16, 11]. The second kind of transition involves the same mechanism, but the transition is due to the non-linearity associated with the physics of the problem. Some explanations for this behavior include non-normality [26], hysteresis [23] or the nature of the flame-acoustic describing-function [27].

Most of the above studies deal with a single fuel, and the conditions used to initiate the transition involve changing either the equivalence ratio or flow speed. Some work also looks at the effect of fuel structure and inlet reactant temperature. For oxy-combustion, fuel and air are expected to be in stoichiometric or near stoichiometric proportions, so it remains to be seen whether there is a fundamental property that can predict mode transitions. For natural gas-air mixtures, Fritsche and coworkers [9] proposed a Damkohler number that non-dimensionalizes the effect of flow velocity on mode transitions. Work with synthesis-gas fuel blends showed that the transitions occur for critical values of a non-dimensional strained flame consumption speed [30, 12]. It was shown that, for a given equivalence ratio and flow velocity, changing the CO:H_2 ratio of the fuel impacts the stability characteristics and mode transition, although the variation in adiabatic flame temperature (T_{ad}) is small. For a given equivalence ratio, changing the fuel composition from 80:20 H_2:CO to 20:80 changes T_{ad} by roughly 100K and drastically alters the stability of the combustor. However, such a change in stability cannot be reproduced if T_{ad} is increased for a fixed fuel composition by raising the equivalence ratio. It appears then that the key parameter that predicts the mode switch is another combustion property such as the consumption speed. The prediction of mode-switching based on a strained flame consumption speed works well for hydrogen enriched mixtures, where the flame speed incorporates the fundamental characteristics of hydrogen such as high diffusivity and unique kinetics.

Little work has been done on oxy-fuel combustion issues in gas turbines until recently [17, 21]. However, a number of groups have begun presenting experimental data. Ditaranto et al. [7] presented acoustic mode results from a 2 kW premixed, expansion-stabilized combustor. Williams et al. [33] used a premixed, 20 kW swirl-stabilized combustor to show that CO emissions do not become significant until an equivalence ratio greater than 0.95 for oxy-combustion, and at this point CO emissions rise more quickly for oxy-combustion than air. Amato et al. [2, 3] used a combustor built the same as Williams' and showed that high equivalence ratio and temperature are associated with excessive CO. They also discussed ways diluents can impact

the flame, such as mixture specific heat (which affects flame temperature), transport properties (thermal conductivity, mass diffusivity,viscosity), chemical kinetic rates (both CO_2 and H_2O are both chemically active), and radiation. Kutne et al. [17] used a 30 kW partially premixed swirl-stabilized combustor at atmospheric pressure, experiencing thermo-acoustic instabilities over a substantial range of operating conditions. They stated a higher sensitivity in performance to oxygen concentration than equivalence ratio. Other bench scale tests have been conducted, such as Glarborg et al. [13] with a 0.1 kW isothermal reactor. They discussed chemistry, stating that CO_2 competes with O_2 for H via CO_2+H$\Leftrightarrow$CO+OH, while CO_2+O$\Leftrightarrow$CO+O_2 and CO_2+OH$\Leftrightarrow$CO+HO_2 are relatively slow. Liu et al. [24] also showed numerically that the overall reaction rate of $CH_4/O_2/CO_2$ mixtures is much slower compared to $CH_4/O_2/N_2$ mixtures primarily because of the competition for the H radical. The demonstration of these effects on flame speed date to Law et al. [36], who showed experimentally that methane flames burning in oxygen-CO_2 mixtures have laminar burning velocities approximately one eighth of those burning in air when the oxygen mole fraction is kept at 21%.

A useful reference for comparing oxy-combustion and air combustion is the adiabatic flame temperature. Although there is an extra degree of freedom in mixture composition by controlling the amount of diluent in oxy-combustion, near-stoichiometric conditions are desired to avoid any excess oxygen in the combustion products. Therefore in Figure 1-1 air combustion temperature is plotted versus equivalence ratio, and stoichiometric oxy-combustion temperature is plotted versus a reversed and shifted axis of diluent CO_2 mole fraction in the $CH_4/O_2/CO_2$ mixture or O_2 mole fraction in the O_2/CO_2 mixture to make comparisons convenient. To be clear, the reactant mixtures are $\phi CH_4 + 2(O_2 + 3.76\ N_2)$ for air and $CH_4 + 2O_2 + \alpha CO_2$ for oxy-combustion, where ϕ and α are varied. The adiabatic flame temperature given is the calculated equilibrium temperature for the reactant inlet temperature at 300 K. In this document, the mole fraction of CO_2 is defined as the mole fraction in the reactant mixture, not the mole fraction in O_2 plus CO_2. The latter is the custom among the coal-combustion community. For reference, however,

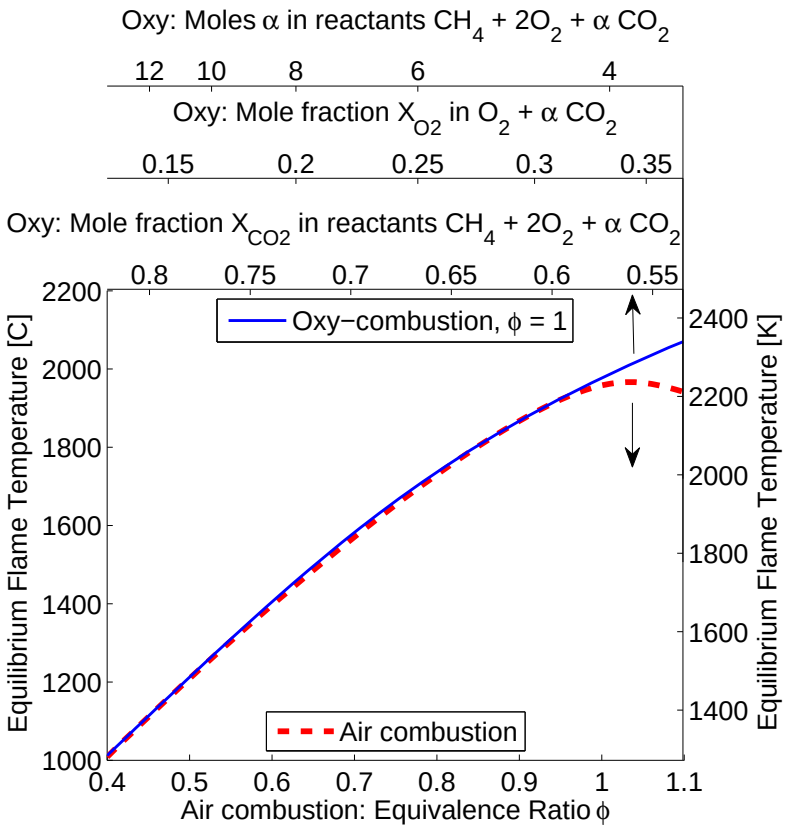

Figure 1-1: Adiabatic (equilibrium) flame temperature comparison for air and oxy-combustion.

the mole fraction of O_2 in O_2 plus CO_2 is also shown.

Because T_{ad} is used often throughout this document, it will be helpful to reference Table 1.1 for reactant conditions at 100 K intervals. The value for α is the number of moles added to the reactants CH_4 + $2O_2$. Since ϕ_{OXY} is unity in this case, X_{CO_2} is simply $\frac{\alpha}{3+\alpha}$.

1.3 Thesis Goals

Successful implementation of oxy-combustion technology requires addressing two challenges concerning the aerothermodynamic design of the combustor. First, the substitution of nitrogen with carbon dioxide as a diluent alters the thermodynamics,

Table 1.1: Mixture reference conditions at T_{ad}

	AIR	OXY, ϕ=1	OXY, ϕ=1
T_{ad} [K]	ϕ	α	X_{CO_2}
1600	0.562	9.28	0.756
1700	0.617	8.27	0.734
1800	0.674	7.38	0.711
1900	0.734	6.56	0.686
2000	0.798	5.80	0.659
2100	0.868	5.08	0.629
2200	0.956	4.38	0.593

transport properties and relative importance of chemical pathways of the reacting mixture, impacting the flame temperature and stability of the combustion process. Second, as in air combustion, the flue gas stream must contain minimal emissions and trace gases, particularly carbon monoxide, nitric oxide and, in the case of oxy-combustion, oxygen. However, the goal of this work is not to design gas turbines; rather, the aim is to characterize oxy-combustion at a fundamental level.

Chapter 2 describes the experimental setup, instrumentation and diagnostics. In Chapter 3, a one-dimensional strained flame code is used to gain insight into turbulent combustion of methane in air and oxy-combustion environments and illustrate the differences between CH_4/air and $CH_4/O_2/CO_2$ flames. Chapter 4 presents experimental data on dynamic mode transitions for oxy-fuel combustors. The broader objective of this effort is to explore the dynamic stability characteristics of oxy-combustion and to compare the characteristics of oxy-combustion and air combustion in order to develop predictive tools for combustor design and retrofit. Results are compared to CH_4/air mixtures for a range of Reynolds numbers. This chapter is closed with a brief overview of the non-linear behavior of the stability characteristics. Chapter 5 presents results for an open-exhaust configuration which removes thermoacoustic instabilities and facilitates the study of fundamental characteristics such as flame structure, flow structure, and blowoff. Finally, Chapter 6 summarizes this work and provides recommendations for future research.

A list of symbols used throughout this document is given in Table 1.2.

Table 1.2: Nomenclature

T_u	Unburned (reactant) temperature
T_{ad}	Adiabatic flame temperature
ϕ	Equivalence ratio
α	Moles of CO_2
X_{CO_2}	Mole fraction CO_2 in reactants (including fuel)
a	Strain rate
S_L	Laminar burning velocity
S_c	Flame consumption speed
v_b	Mean inlet velocity at blowoff

Chapter 2

Experimental Setup

2.1 Equipment

The combustor, shown in Figure 2-1, is designed to stabilize combustion using a combination of swirl and sudden expansion. Premixed $CH_4/O_2/CO_2$ or premixed CH_4/air enters the combustor through a 38 mm diameter inlet pipe. The swirler is located 5 cm upstream of the expansion plane and has 8 blades with an estimated swirl number of 0.53 [19]. The swirler can also be moved flush with the dump plane, which has an effect on the dynamics, but this was found to cause excessive heating of the swirler. From the expansion plane downstream, the inner diameter is 76 mm. The first 40 cm downstream where the flame is anchored consists of a quartz tube for optical access. The overall acoustic length of the combustor (from the choke plate to the end of exhaust tube) is 4.5 m. The flow is choked upstream to prevent equivalence ratio oscillations and provide a known acoustic boundary condition ($u' = 0$).

Air, CO_2, O_2, and CH_4 are each supplied using Sierra Instruments mass flow controllers capable of supporting a thermal power of 50 kW. The accuracy of each is +/- 1% of full scale with a repeatability of +/- 0.2% of full scale, but special note should be made here of issues with the flow accuracy. Another piece of Sierra equipment, a 780s flow meter, was used to find a proportional offset for the air flow controller such that (actual flow rate) = 0.96∗(apparent flow rate). During oxy-combustion, CO_2 flows through the same controller; however, the correction factor

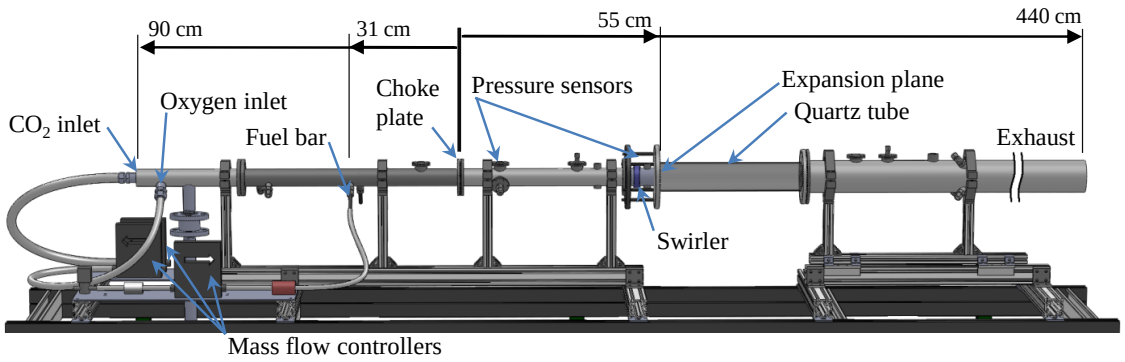

Figure 2-1: Model of axisymmetric swirl combustor.

is not used for the CO_2 flow rate because additional calibration equipment would be required. An additional zero offset correction of 3.9 standard liters per minute of CH4 is used for the fuel mass flow controller. The flow rate of O_2 in the third controller, used only in oxy-combustion, is assumed to be within the specified accuracy.

Two Kulite MIC-093 pressure transducers are used to record pressure oscillations 11 cm and 52 cm downstream of the choke plate at 10 kHz.

For the chemiluminescence images presented in Sections 4.1 and 4.2, high speed images are recorded at 500 fps using a MEMRECAM GX-1 high speed camera fitted with a 50mm f/1.8 lens. A 2mm thick CG-BG-39 Schott-glass is placed in front of the camera to block out infrared radiation. The field of view in all the images starts at the dump plane of the combustor and extends about 22.8 cm downstream. Images are post-processed by normalizing the intensities in each image with the maximum intensity of the brightest image in an instability cycle.

A model of the swirler is shown in Figure 2-2. While premixed combustion is the focus of this work, an injection tube was installed through the centerbody of the swirler in order to try non-premixed combustion, as shown in Figure 2-3. This resulted, however, in long flames with bright, even sooty tips. The reason for this undesirable flame behavior is likely due to excessive jet penetration of the fuel through the inner recirculation zone due to high fuel to oxidizer velocity ratios, affecting the flow structure and mixing significantly. Therefore, only premixed combustion is presented for the given geometry. Even with the tubing through the centerbody, the

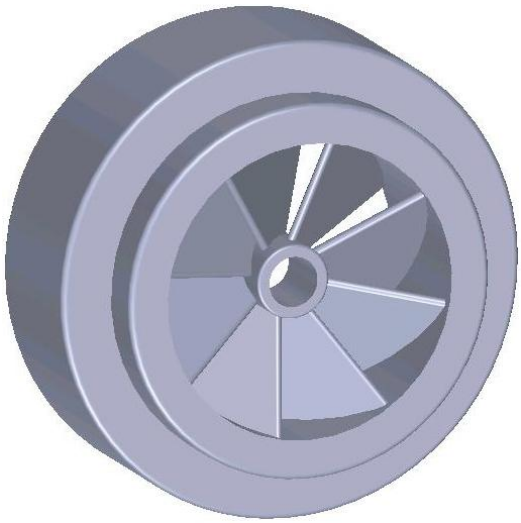

Figure 2-2: Model view of swirler. The inside diameter of the flow area is 1.5 inches. A fuel injection tube is inserted through the centerbody for non-premixed combustion capability.

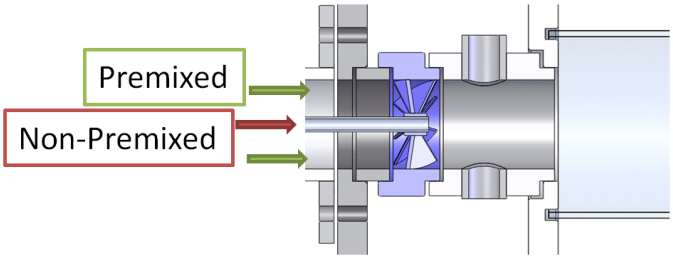

Figure 2-3: Cutaway view of swirler and expansion plane zone showing plumbing for premixed and non-premixed combustion.

centerbody acts as a small bluff body because there is no flow through the tube for premixed combustion.

Another hardware switch that can be toggled is the exhaust configuration. Shown in Figure 2-4 (a), the closed exhaust configuration is used to study combustion dynamics (Chapter 4) with the previously described acoustic length of 4.5 m. The second configuration, shown in (b), consists of an open exhaust annulus at the end of the quartz tube. With the acoustic length significantly shortened, phenomena such as blowoff can be studied without combustion dynamics (Chapter 5). The blue arrows indicate room air that is drawn into the exhaust at room pressure.

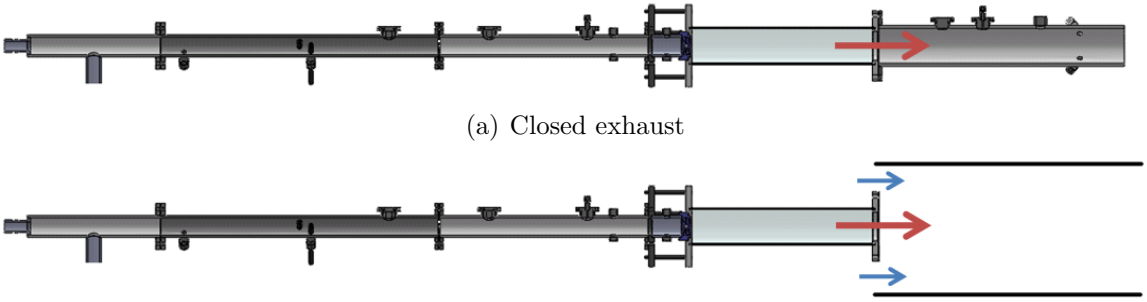

(a) Closed exhaust

(b) Open exhaust

Figure 2-4: (a) Closed exhaust configuration for studying combustion dynamics and (b) open exhaust configuration to remove instabilities.

2.2 MATLAB Code

A custom Matlab code is used for control, data acquisition, and processing. The control portion includes a graphical user interface which communicates with the mass flow controllers via COMM ports. Digital outputs (fuel shutoff solenoid valve, camera and PIV triggering) and analog inputs (thermocouples, pressure transducers, photomultiplier tube) are fed through an NI BNC-2110 connector block and an NI PCIe-6259 data acquisition card. The interface allows a flow parameter to be chosen to hold constant during tests. For all runs presented in this work, Reynolds number is held constant and temperature is varied by changing ϕ in air combustion and X_{CO_2} in oxy-combustion. Mean inlet velocity, total mass flow rate, and power output are all dependent variables. During operation, live plots of all flow rates and an FFT of the pressure signal are displayed to monitor dynamic modes. Data can be logged in multiple sessions without restarting the combustor.

In each test which sweeps across temperature, the set conditions (flow rates) are held constant for a few seconds before switching ϕ or X_{CO_2} to the next set temperature. The processing code then looks for periods of time in which the flow conditions are constant within a specified tolerance and produces an output for each. These outputs are binned and reduced to plots such as the ones shown in Figure 4-8.

2.3 Operating Conditions

Shown in Figure 2-5 are the approximate operating ranges for the combustor in air and oxy-combustion modes. The purpose of this plot is to display the conditions of operation because a basis of comparison must be established for the two modes. The flame is generally ignited and brought near 2200 K. Next, the temperature (and power) are gradually reduced along the line of constant Re for the Reynolds number at which the combustor is ignited. The lower temperature limit determined by blowoff, generally between 1600 K and 1700 K.

For a given Reynolds number and adiabatic flame temperature, the power output of oxy-combustion is lower. For example, at Re = 20,000 and T_{ad} = 1800 K, the fuel flow rate for oxy-combustion is 0.37 g/s, while the fuel flow rate is 0.44 g/s for air. Likewise, the total mass flow rate and mean inlet velocity are lower for oxy-combustion at 9.4 g/s and 5.2 m/s versus 10.8 g/s and 8.0 m/s for air. In air combustion, the mean inlet velocity change is small when the equivalence ratio is changed to adjust the temperature at constant Reynolds number. However, the mean inlet velocity changes more significantly in oxy-combustion at constant Reynolds number when changing the temperature because the bulk properties change with X_{CO_2}. One should also consider which parameters are varied with varying load (turn-down ratio) in gas turbine operation.

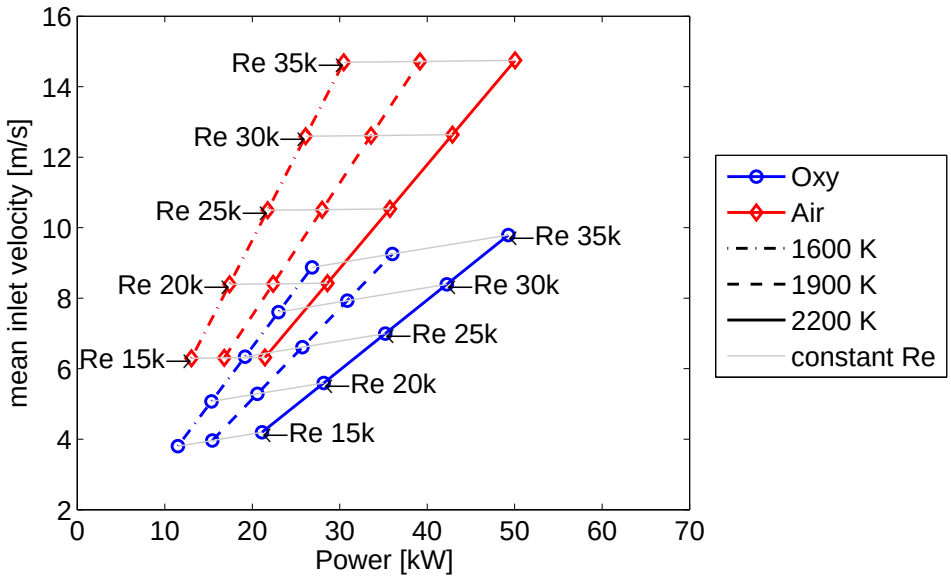

Figure 2-5: Constant temperature contours at three arbitrary temperatures for the combustor in air and oxy-combustion as a function of thermal power output for different Reynolds numbers at $T_u = 300$ K. In oxy-combustion, $\phi = 1$ and CO_2 dilution is varied. In air combustion, $\phi < 1$. Note that blowoff actually occurs before 1600 K is reached in constant Reynolds number tests (see Chapter 5). This plot applies to both exhaust configurations shown in Figure 2-4.

Chapter 3

Numerical 1-D Strained Flame

As discussed in Chapter 1, the laminar burning velocity of $CH_4/O_2/CO_2$ mixtures are one eighth of CH_4/air mixtures for an oxygen mole fraction of 21%. For these mixtures the oxy-combustion flame temperature is much lower due largely to the roughly 65% larger heat capacity of CO_2 on a molar basis. The interest, however, is in comparing flames at the same flame temperature, and the difference in burning velocity is still significant. Given that flames in turbulent flows are subjected to strains, the interest is in computing the strained flame consumption speed. This provides the mixture fractions of CO_2 for which the strain rates anticipated in experiments exceed the extinction strain rates for oxy-fuel mixtures.

3.1 Numerical Setup

A one-dimensional strained flame code is used to compute the consumption speed for varying strain rates. The laminar flame is stabilized in a planar stagnation flow and shown in Figure 3-1, where the opposed twin flame configuration allows extinction to occur at higher strain rates when the flames are pushed closer together. The resultant potential flow velocity field is characterized by the strain rate parameter a. The stretch rate κ of the planar flame under steady conditions is simply $\kappa = a$.

Governing equations for the flame structure are found by using a boundary layer approximation across the flame thickness. CHEMKIN and TRANSPORT libraries

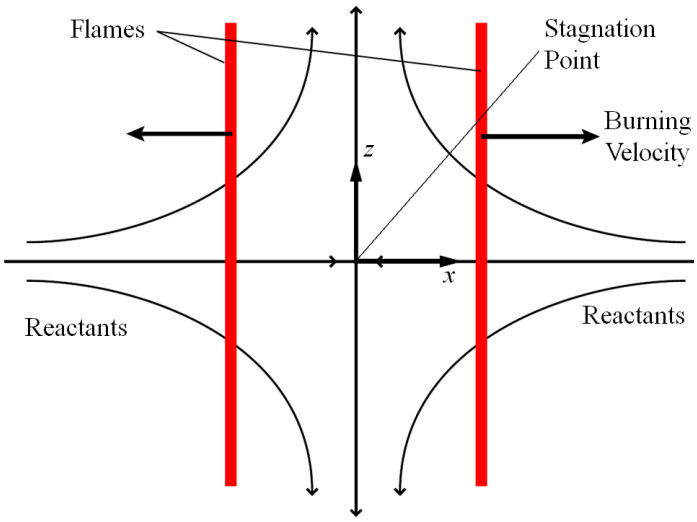

Figure 3-1: Twin Flame configuration for 1-D strained flame simulation. This configuration allows extinction to occur when the strain rate is high enough that the flame front is pushed close to the stagnation point.

are used to evaluate chemical source terms and the various physical properties. A modified version of the GRI-Mech 3.0 kinetic model is used where the nitrogen-containing species have been removed except for N_2 in the air cases. Radiation effects are not considered in the model. Further details of the model can be found in Speth et al. [31]. The consumption speed S_c of the flame is defined as

$$S_c = \frac{\int_{-\infty}^{\infty} q'''/c_p \, dx}{\rho_u (T_b - T_u)}$$

where q is the volumetric heat release rate, c_p is the specific heat of the mixture, x is the coordinate normal to the flame, ρ_u is the unburned mixture density, and T_u and T_b are the unburned and burned temperature, respectively. Extrapolating the consumption speed to a strain rate of zero gives the laminar burning velocity.

All cases are at atmospheric pressure, and the reactant temperature is 300 K in all cases except as described in Figure 3-4. The proper mixture compositions for the given adiabatic flame temperatures are calculated using CANTERA with GRI-Mech 3.0 by equilibrating the mixture at constant enthalpy and pressure (complete combustion is not assumed).

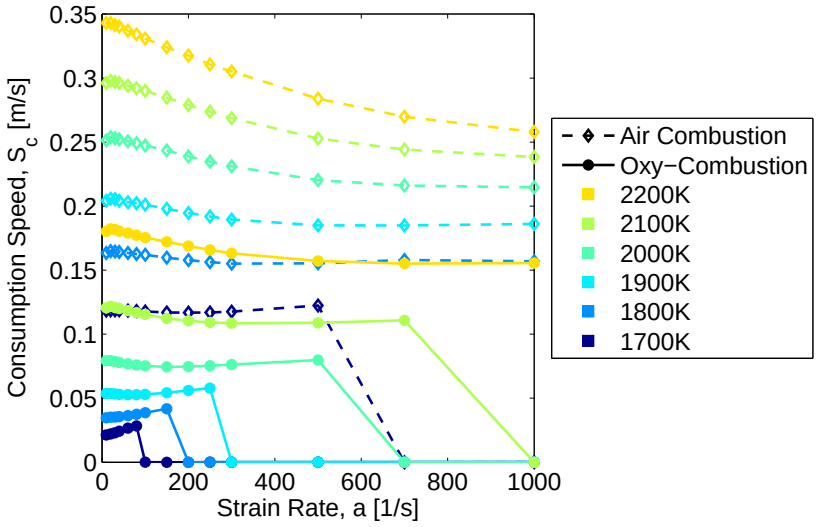

Figure 3-2: Consumption speed vs strain rate a for $T_{ad}s$ from 1700 K to 2200 K, where $T_u = 300$ K. The oxy-combustion equivalence ratio is $\phi = 1$.

3.2 Flame Consumption Speed

The consumption speed at a given strain rate for a mixture is one of the major outputs of interest, and the differences between air and oxy-combustion are significant. Shown in Figure 3-2 are consumption speeds for air and oxy-combustion at equal adiabatic flame temperatures from 1700 K to 2200 K. Here again ϕ in air combustion and α in oxy-combustion are varied to change T_{ad}. At 2200 K the consumption speed of the oxy-combustion flame is roughly half that of air. At lower temperatures the difference is more extreme, where oxy-combustion consumption speed is less than 5 cm/s, or one fourth that of air. Clearly the substitution of N_2 with CO_2 in the oxy-combustion flames adversely affects the chemical and/or transport time scales.

Also important in characterizing flame behavior is the condition at which extinction occurs. Instances of extinction (five for oxy, one for air) are shown in Figure 3-2 where the consumption speed drops to zero. Since strain rates on the order of 250 s^{-1} are expected in the experiments for similar conditions [30], sustainable oxy-combustion flames are not expected to exist at or below 1800 K. As will be shown though, experimental flames exist at temperatures well below this value. One possible

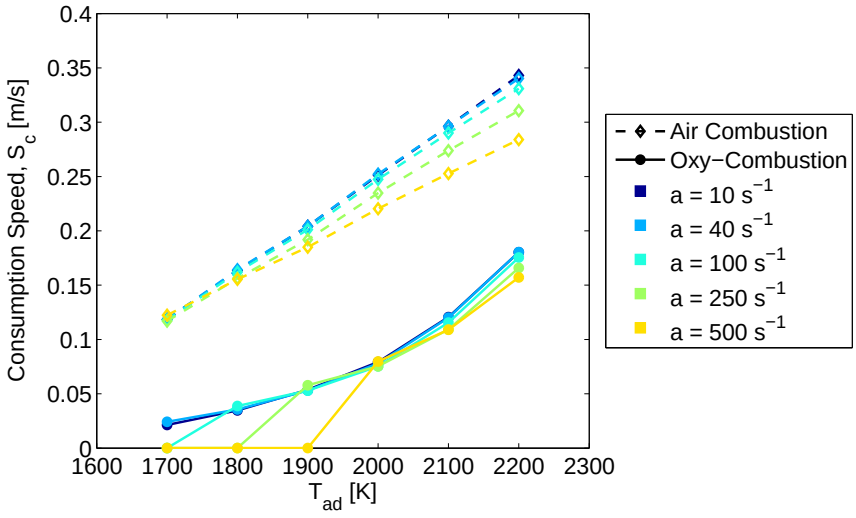

Figure 3-3: Consumption speed vs T_{ad}, where $T_u = 300$ K. The oxy-combustion equivalence ratio is $\phi = 1$.

reason is the turbulent effects of local mixing on pockets of products and reactants. Taking the information from Figure 3-2 and plotting S_c against temperature for selected strain rates in Figure 3-3, one can see the near linear dependence of S_c on temperature for air combustion and a non-linear dependence for oxy-combustion.

Since one might ideally wish to compare premixed oxy-combustion to lean premixed air combustion, consumption speed comparisons are also made for an adiabatic flame temperature of 1400°C. In these cases, the reactant temperature is varied from 300 K to 800 K, and the equivalence ratio in air combustion and the CO_2 mole fraction in oxy-combustion are still varied to maintain an adiabatic flame temperature of 1400°C. This temperature is suitable for gas turbines which operate under load at an equivalence ratio near 0.6 to achieve low NO_x emissions and to stay within the material limitations of the turbine. Therefore, results from the 1-D strained flame code at 1400°C are shown in Figure 3-4, and the difference between air and oxy-combustion is drastic. Even when the oxy-combustion mixture is preheated to 800 K, the consumption speed is still well below that of air for a reactant temperature of 300 K.

Extrapolating the consumption speed as the strain rate goes to zero, one can

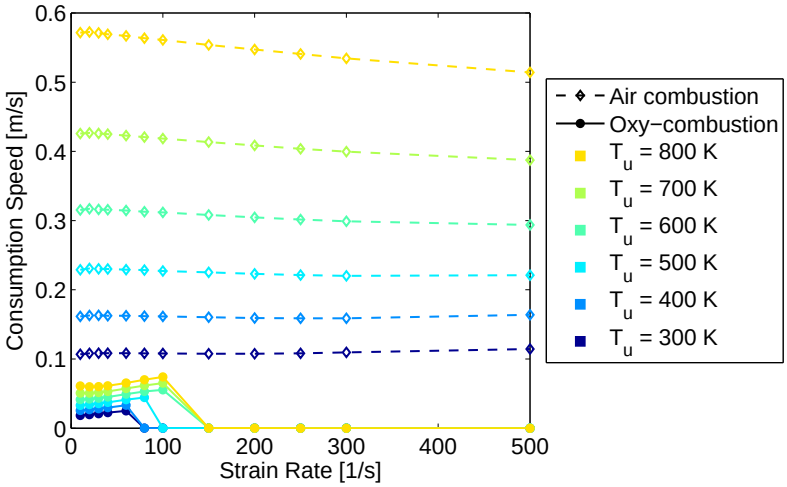

Figure 3-4: Consumption speed vs strain rate a for T_{ad}=1400°C, where T_u ranges from 300 to 800 K. The oxy-combustion equivalence ratio is $\phi = 1$.

obtain the laminar burning velocity (S_L). The laminar burning velocity has been shown to be significantly lower for methane oxy-combustion, both for varied equivalence ratio at 21% O_2 in the oxidizer and for stoichiometric CO_2 dilution compared to stoichiometric N_2 diluted mixtures for varied dilution amounts (see Chen et al. [5]). What is novel, however, is to plot laminar burning velocity as a function of adiabatic flame temperature as shown in Figure 3-5. Interestingly, S_L appears linear for air combustion, while S_L increases more quickly at higher temperatures for oxy-combustion. These values of S_L match well with values from a similar CHEMKIN model.

In addition to plotting stoichiometric oxy-combustion in Figure 3-5, oxy-combustion for an equivalence ratio of 0.95 is also plotted at the same temperatures. This means that at $\phi = 0.95$, slightly fewer moles of CO_2 are required to obtain products at the same temperature in the reactants $\phi CH_4 + 2O_2 + \alpha CO_2$. The laminar burning velocity is a small amount higher for $\phi = 0.95$, presumably because the adverse effects of CO_2 on chemical time scales is lower. This upward trend in S_L for decreasing equivalence ratio at constant (fixed) T_{ad} for oxy-combustion can be continued, and is shown in Figure 3-6. The curve represents a vertical slice from Figure 3-5 at T_{ad} = 1800 K. Moles α of CO_2 are decreased as ϕ is decreased from unity on the right

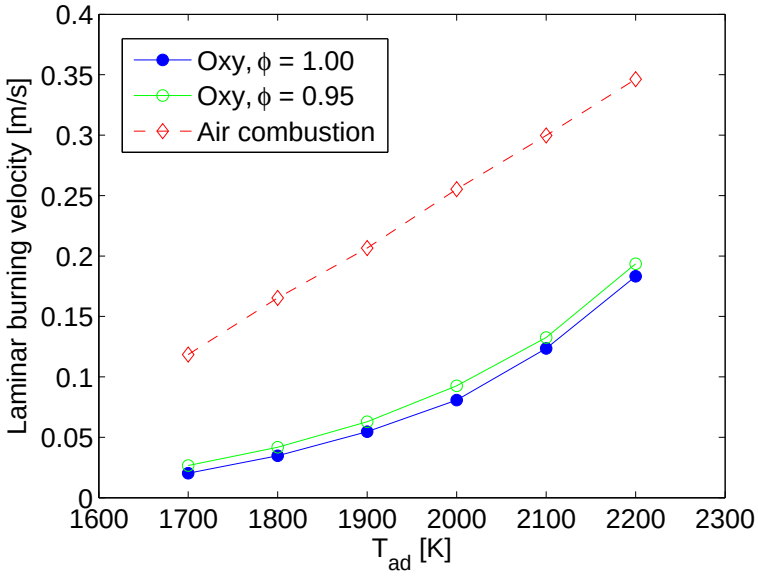

Figure 3-5: Laminar burning velocity vs adiabatic flame temperature for $T_u = 300$ K.

to $\phi = 0.148$ on the left. At this minimum equivalence ratio for combustion at 1800 K, there is no carbon dioxide, and the reactants are only methane (0.148 moles) and oxygen (2 moles).

Because of the low flame speeds in oxy-combustion, proportionally larger flame areas should be required for wrinkled laminar flames, and long, weak flames are expected. However, shown in Figure 3-7 is the effective required area for a wrinkled flame, comparing air and oxy-combustion at the same Reynolds numbers for three temperatures. This flame area is given by $A = \frac{\dot{m}}{\rho_u S_L}$, where $\dot{m}$, ρ_u, and S_L are the total mass flow rate, unburned gas density, and laminar burning velocity for the mixture, respectively. At 2200 K, the area needed for oxy-combustion is only 25% higher than air. Furthermore, images in Chapter 4 from high speed video show a remarkable similarity with air combustion in not only flame structure but also flame size. At lower temperatures, though, the theoretical area is several times larger for oxy-combustion.

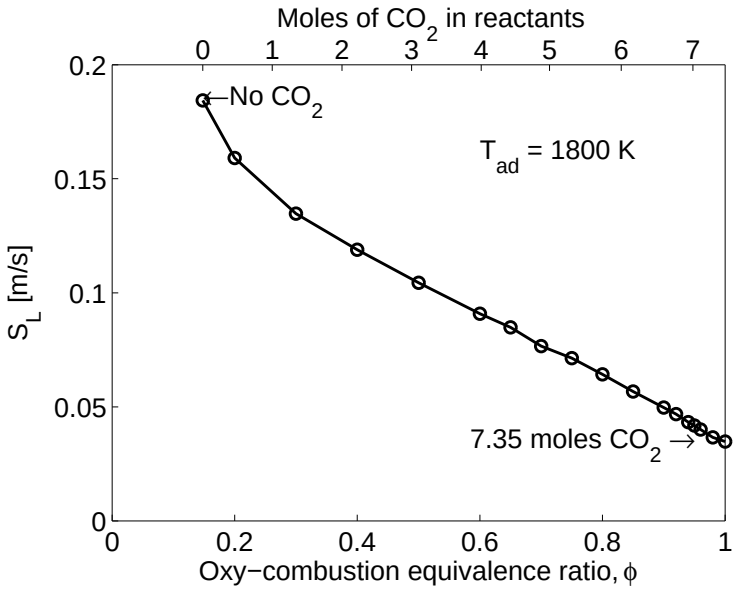

Figure 3-6: Laminar burning velocity vs oxy-combustion equivalence ratio for T_u = 300 K. To keep T_{ad} constant at 1800 K, the amount of CO_2 dilution is varied from zero at ϕ=0.148 to the highest amount at ϕ=1.0.

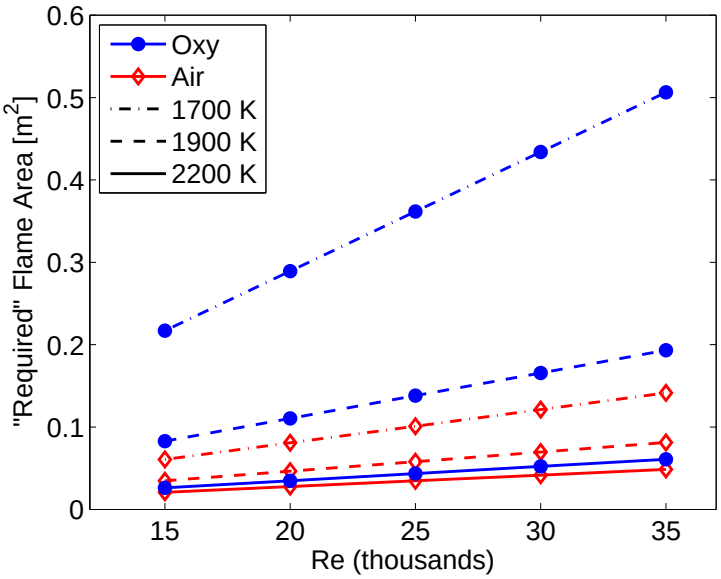

Figure 3-7: Flame area based on S_L, where T_u = 300 K. The oxy-combustion equivalence ratio is $\phi = 1$.

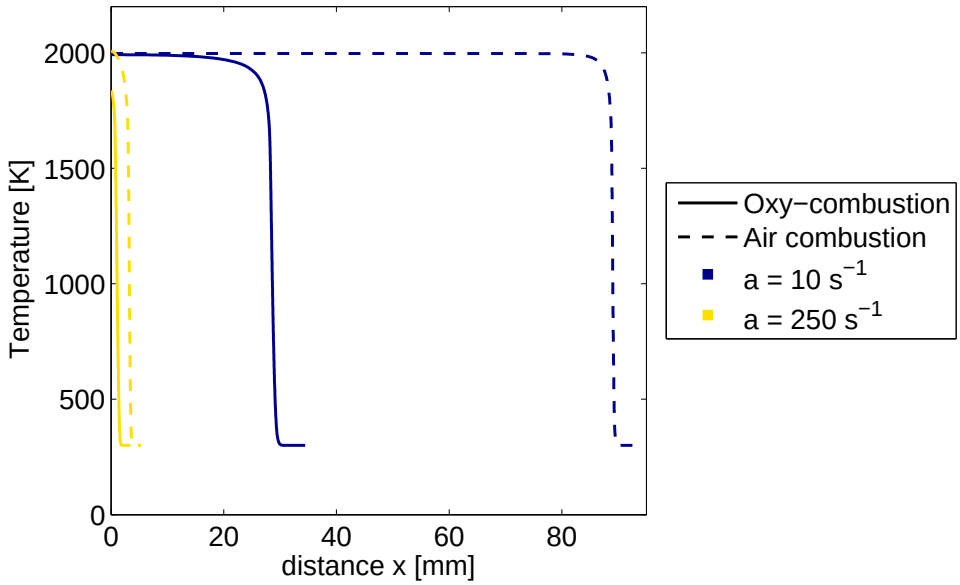

Figure 3-8: Temperature profiles at $a = 10$ and 250 s^{-1} for $T_{ad} = 2000$ K, where $T_u = 300$ K. The oxy-combustion equivalence ratio is $\phi = 1$.

3.3 Temperature and Species Profiles

Basic outputs of the strained flame code that provide insight into flame characteristics include temperature and species profiles. Shown in Figure 3-8 are temperature profiles for air and oxy-combustion for two strain rates at a set $T_{ad} = 2000$ K. Following the flow from right to left, toward the stagnation point at $x = 0$, reactants enter at 300 K. Next, in the reaction zone, the temperature rises steeply to the burned gas temperature. The distance of the flame from from the stagnation point is the steady-state distance for the flame at a given strain rate. For both strain rates, the CH_4/air flame resides at a greater distance from the stagnation point because of the higher consumption speed. At $a = 250s^{-1}$, the flames are "pushed" closer to $x = 0$. To see the temperature profiles more clearly at $a = 250s^{-1}$, refer to Figure 3-10.

Shown in Figure 3-9 are species profiles of O_2, CH_4, CO, and CO_2 for two strain rates which correspond to the temperature profiles in Figure 3-8. In oxy-combustion, the amount of incoming fuel is half the amount of oxygen due to the stoichiometric mixture, while the amount of fuel in air combustion is less than half the amount of

oxygen because $\phi = 0.8$. One can also get a feel for the amount of CO_2 that would need to be recycled from the products in reality to obtain the desired inlet conditions, for this case about 87%. At the higher strain rate of 250 s^{-1}, the effect of stretch becomes apparent in oxy-combustion from the significant amount of oxygen left over and excessive CO remaining by the time the mixture reaches the stagnation point. Also note the difference in x-axis scales in Figure 3-9 (a) and (b).

Next, an example case is explored for profiles at a single strain rate of 250 s^{-1} and two temperatures in order to demonstrate the importance of temperature. The products of air and oxy-combustion shown, in Figure 3-10, each reach their set temperature at 2200 K, but oxy-combustion at 2000 K falls short by 165 K. This is evidence of a weak flame with partial extinction, and the impact on CO levels is shown in Figure 3-11. Each of the CO "outputs" at the stagnation plane overshoots the equilibrium value. For instance, oxy-combustion CO at 2200 K overshoots by 50%, but at 2000 K the overshoot is 400% due to the incomplete combustion. To glean some information on the chemical impact of CO_2 without a detailed chemical analysis, consider Figure 3-12. Noting the air and oxy-combustion curves at $T_{ad} = 2200$ K, where both reach the set T_{ad}, the relative peak heights of H and OH can be viewed as a demonstration of competition for the H radical in CO_2+H$\Leftrightarrow$CO+OH. More H is consumed via the reaction in oxy-combustion due to the presence of CO_2, resulting in lower ppm values of H and higher values of OH as well as CO.

3.4 Emissions Considerations

Rather than NO_x and CO as the emissions of interest in air combustion, the most important emissions in oxy-fuel combustion of natural gas are CO and O_2. There is a trade-off between emitting these two species, as shown in Figure 3-13 for varied ϕ in oxy-combustion while holding T_{ad} at 1800 K and a low strain rate of $a = 10s^{-1}$. The values of CO and O_2 shown are the levels in the products when they reach the stagnation point. The crossover point at about $\phi = 0.97$ is similar to that seen experimentally at $\phi = 0.95$ by Li et al. [21]. Williams et al. [33] also experimentally

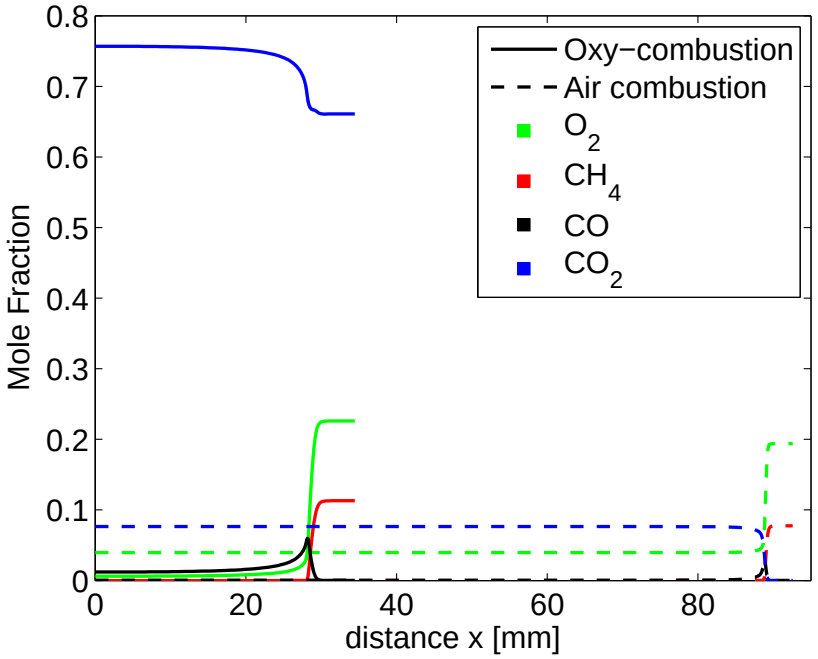

(a) $a = 10s^{-1}$

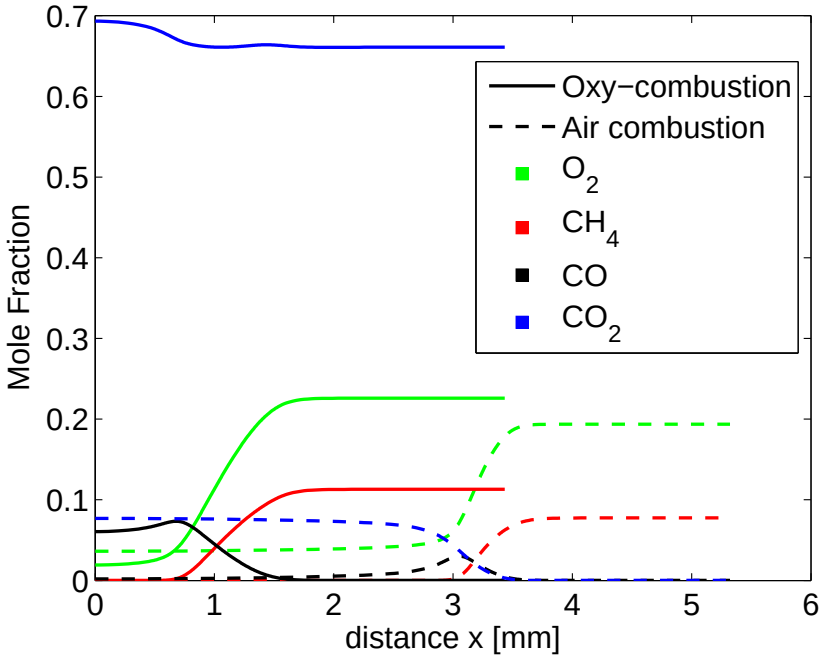

(b) $a = 250s^{-1}$

Figure 3-9: Species Profiles of O_2, CH_4, CO, and CO_2 at (a) $a = 10s^{-1}$and (b) $a = 250s^{-1}$ for air and oxy-combuation at $T_{ad} = 2000$ K. $T_u = 300$ K and the oxy-combustion equivalence ratio is $\phi = 1$.

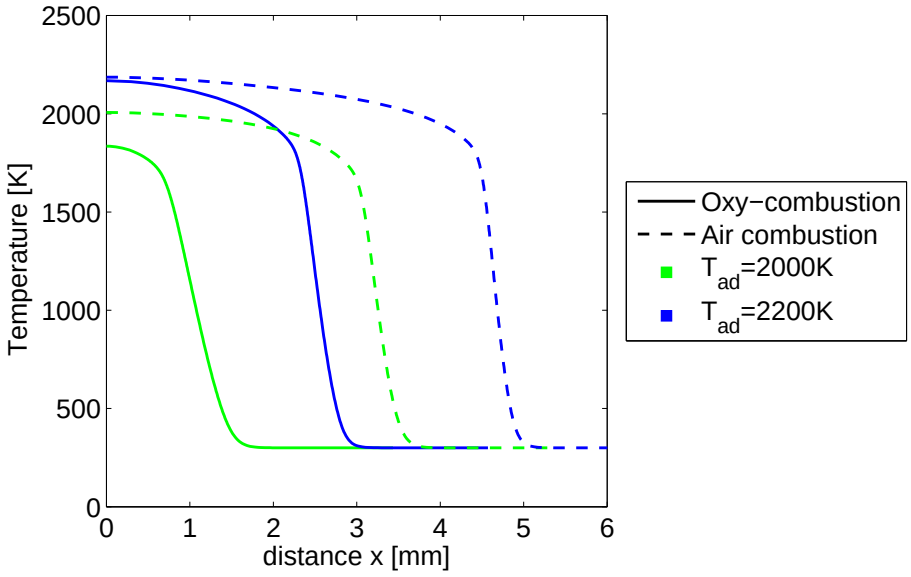

Figure 3-10: Temperature profiles at $a = 250s^{-1}$ for T_{ad}s of 2000 K and 2200 K, where $T_u = 300$ K. The oxy-combustion equivalence ratio is $\phi = 1$.

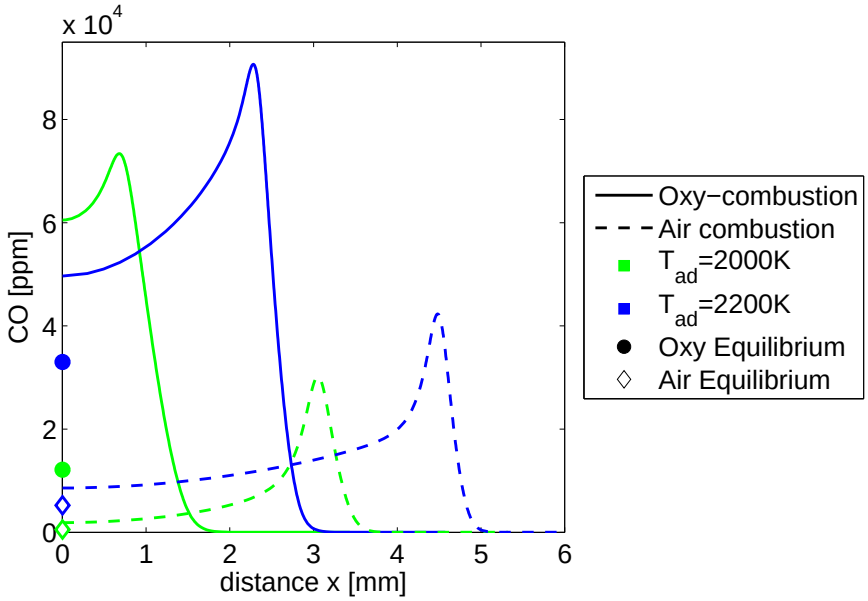

Figure 3-11: CO profiles at $a = 250s^{-1}$ for T_{ad}s of 2000 K and 2200 K, where $T_u = 300$ K. The oxy-combustion equivalence ratio is $\phi = 1$. Point values correspond to equilibrium CO at T_{ad}.

showed surprisingly low CO values until $\phi > 0.95$ for $CH_4/O_2/CO_2$ flames at a fixed O_2 concentration.

Especially at lower temperatures, the equilibrium values of CO for stoichiometric oxy-combustion are orders of magnitude higher than for air combustion. This is the starting point for Figure 3-14, shown with continuous lines. Next, values of CO at the stagnation point are plotted for varied strain rates for set adiabatic flame temperatures from 1700 K to 2200 K. In air combustion, CO values at $a = 10s^{-1}$ nearly match equilibrium, and CO increases much more quickly with strain rate at lower temperatures (kinetic effects). Values for oxy-combustion behave similarly, only with a much higher starting point. It is also interesting to note that for mixtures such that $T_{ad} \leq 1900$ K, CO levels at even the lowest strain rates do not approach equilibrium. Rather, at $T_{ad} = 1700$ K and $a = 10s^{-1}$, CO exceeds 1.5 %. The x-axis values for these points changes with strain because the temperature used is the maximum temperature for that strain rate. Therefore, Lewis number effects (which may also lead to partial extinction effects) are expected to be the cause of this shift in burned gas temperature. Overall, the impact of residence time on CO emissions is important, and the distance at which the flame resides from the stagnation point affects the levels shown.

3.5 Lewis Number Effect

For a positively stretched flame such as the stagnation flame used in this chapter, Law [20] showed that the mixture Lewis number has important effects on properties such as temperature and extinction strain. It is known that $Le < 1$ for methane-air mixtures, and in Figure 3-15, the curves for air combustion at multiple adiabatic flame temperatures are consistent with the curve in [20] for $Le < 1$. The temperature increases slightly with increasing strain until near extinction, where the curve changes concavity and the value decreases. For $Le > 1$, the temperature monotonically decreases with increasing strain. This effect is clearly exhibited at $T_{ad} = 1700$ K, 1800 K, and 1900 K for oxy-combustion. At higher temperatures for oxy-combustion,

however, where there is less CO_2 in the mixture, it appears that the Lewis number increases past unity and begins to behave more like air combustion.

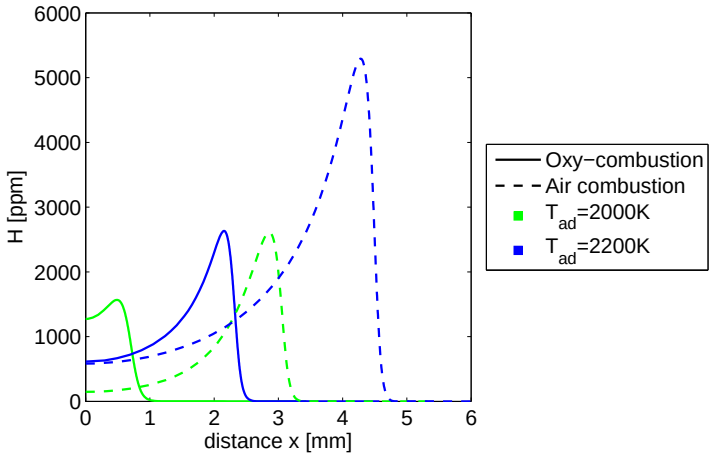

(a) H radical

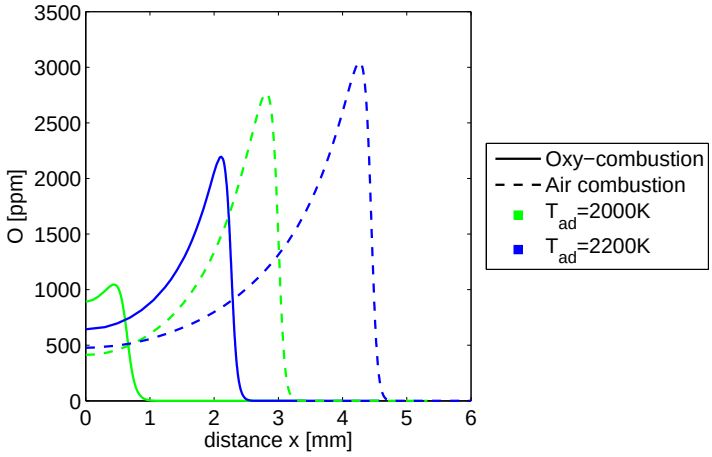

(b) O radical

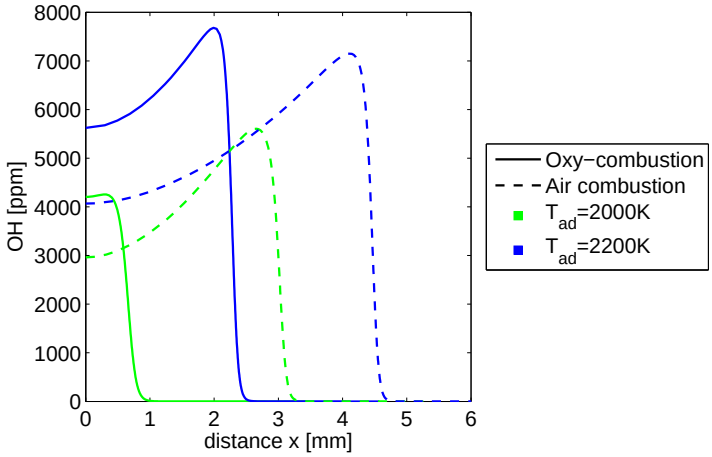

(c) OH radical

Figure 3-12: H, O and OH radical profiles at $a = 250s^{-1}$ for T_{ad}s of 2000 K and 2200 K, where $T_u = 300$ K. The oxy-combustion equivalence ratio is $\phi = 1$.

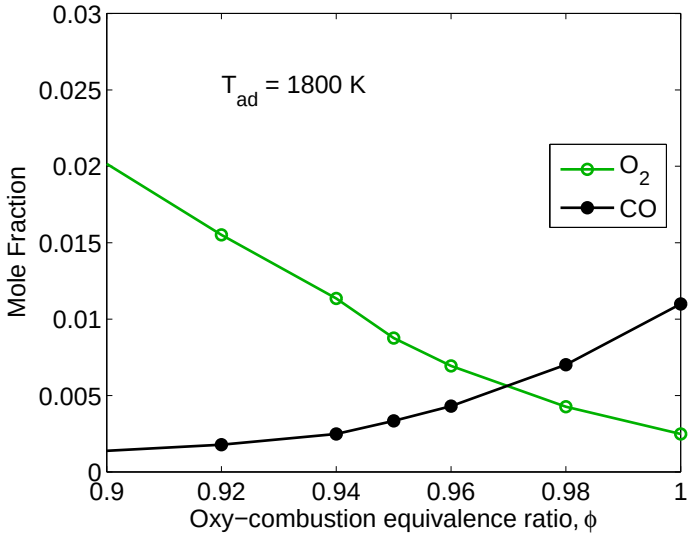

Figure 3-13: O_2 and CO output at constant $T_{ad} = 1800$ K for $T_u = 300$ K. The strain rate is $a = 10s^{-1}$.

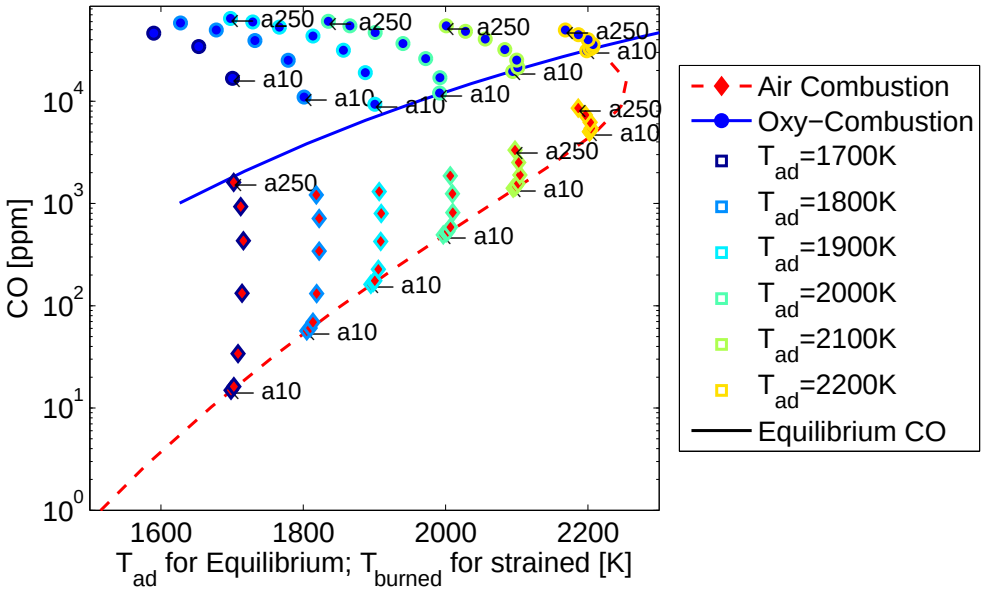

Figure 3-14: CO output vs Temperature for $T_u = 300$ K. Continuous lines are equilibrium values, and points are strained flame values for set values of T_{ad} from 1700 K to 2200 K and strain rates $a = [10\ 30\ 60\ 100\ 150\ 200\ 250]\text{s}^{-1}$. At a given mixture setting (set T_{ad}), the CO output increases with increasing strain, and the actual flame temperature shifts according to Lewis number effects with increasing strain. The oxy-combustion equivalence ratio is $\phi = 1$.

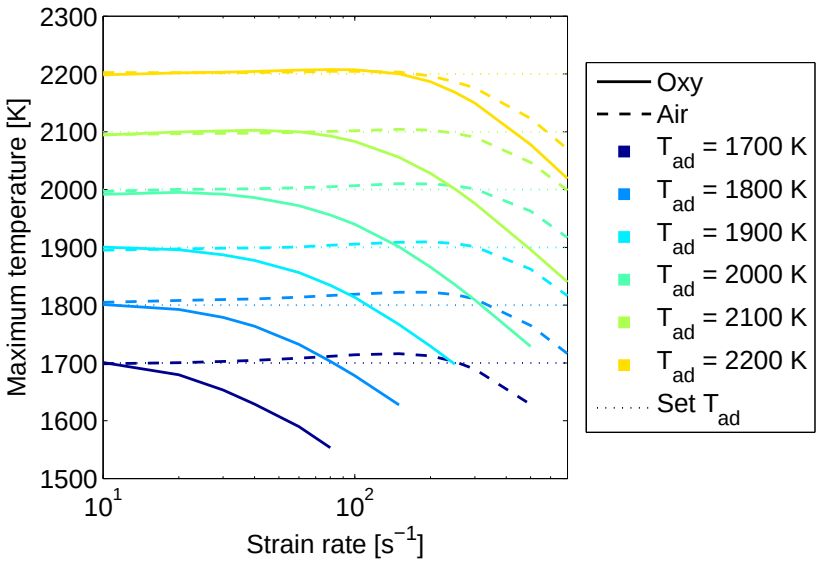

Figure 3-15: Lewis number effect. Maximum flame temperature vs strain rate a for set values of T_{ad} from 1700 K to 2200 K, where $T_u = 300$ K. The oxy-combustion equivalence ratio is $\phi = 1$.

Chapter 4

Combustion Dynamics

This chapter presents results for the combustor described in Chapter 2. In all cases, the Reynolds number is based on the 0.0381 m (1.5 inch) inlet diameter, the mean inlet velocity, and the reactant density and viscosity at 300 K. All oxy-combustion experiments are conducted at $\phi = 1$.

4.1 Oxy-Combustion Baseline Characteristics

To understand the baseline stability characteristics of the combustor, consider Figure 4-1. This figure plots the Overall Sound Pressure Level (OASPL) as a function of CO_2 mole fraction for stoichiometric CH_4/O_2 mixtures at Re = 20,000 for different amounts of CO_2 dilution. The OASPL measurements are taken using the transducer placed just upstream of the expansion plane. In this figure as well other OASPL plots throughout the paper, the symbols have been colored based on the frequency of the instability.

For low dilution levels (T_{ad} = 2230 K), the flame is very compact and the sound pressure levels exceed 160 dB. The dominant instability frequency is 132 Hz, which corresponds to the five-quarter wave mode of the combustor. High speed flame images for this mode show that the flow oscillates between a double-helix type vortex breakdown (as seen visually by experimental observation of flame filaments) and a configuration in which it flashes back (see Figure 4-2).

As the dilution levels are increased, the combustor remains unstable at roughly the same amplitude, though the contribution of the five-quarter wave mode to the OASPL decreases and the three-quarter wave mode (83 Hz) increases.

At $X_{CO_2} = 0.63$ ($T_{ad} = 2100$ K) the combustor abruptly transitions to the three-quarter wave mode while maintaining the same limit-cycle amplitude. High speed images for this condition indicate that the flow-structures are now different, with the flow structures switching between a double-helix type and a spiral type breakdown during the instability cycle (see Figure 4-3). The type of structures observed are surmised visually during experiments.

As the dilution levels are increased from $X_{CO_2} = 0.63$ ($T_{ad} = 2100$ K) to $X_{CO_2} = 0.67$ ($T_{ad} = 1970$ K), the apparent flame length increases, commensurate with what is expected when decreasing the flame temperature. The flame dynamics are controlled by the fluid mechanics of the inner recirculation zone as was reported in work on propane-air mixtures [19].

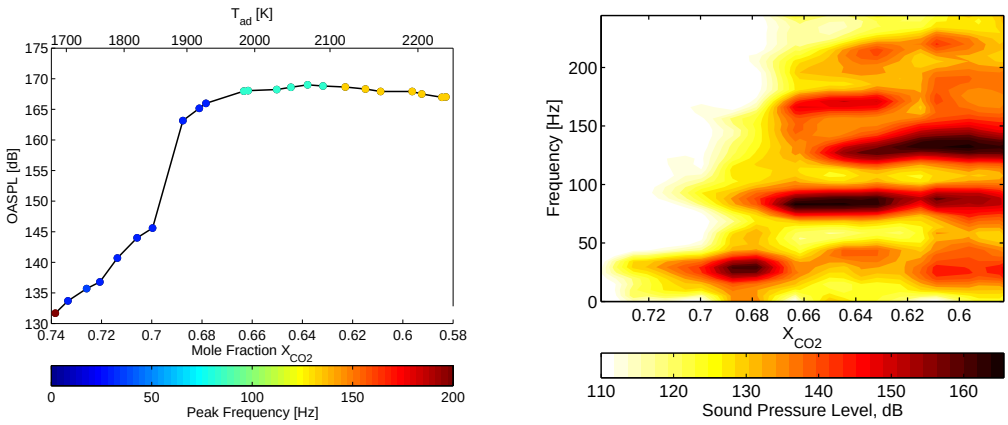

(a) OASPL for $Re = 20{,}000$

(b) Frequency spectrum for $Re = 20{,}000$

Figure 4-1: OASPL (a) and spectrum (b) of oscillations as a function of adiabatic flame temperature for $CH_4/O_2/CO_2$ mixtures at $Re = 20{,}000$. For reference, note the two x-axes in (a).

The next abrupt transition is seen at $X_{CO_2} = 0.67$ ($T_{ad} = 1970$ K) where the instability jumps from the three-quarter wave mode to the quarter wave mode with a slightly lower limit-cycle amplitude. For this case though, there is a step jump in flame length (Figure 4-4). This mode persists until $X_{CO_2} = 0.7$ ($T_{ad} = 1850$ K) when the

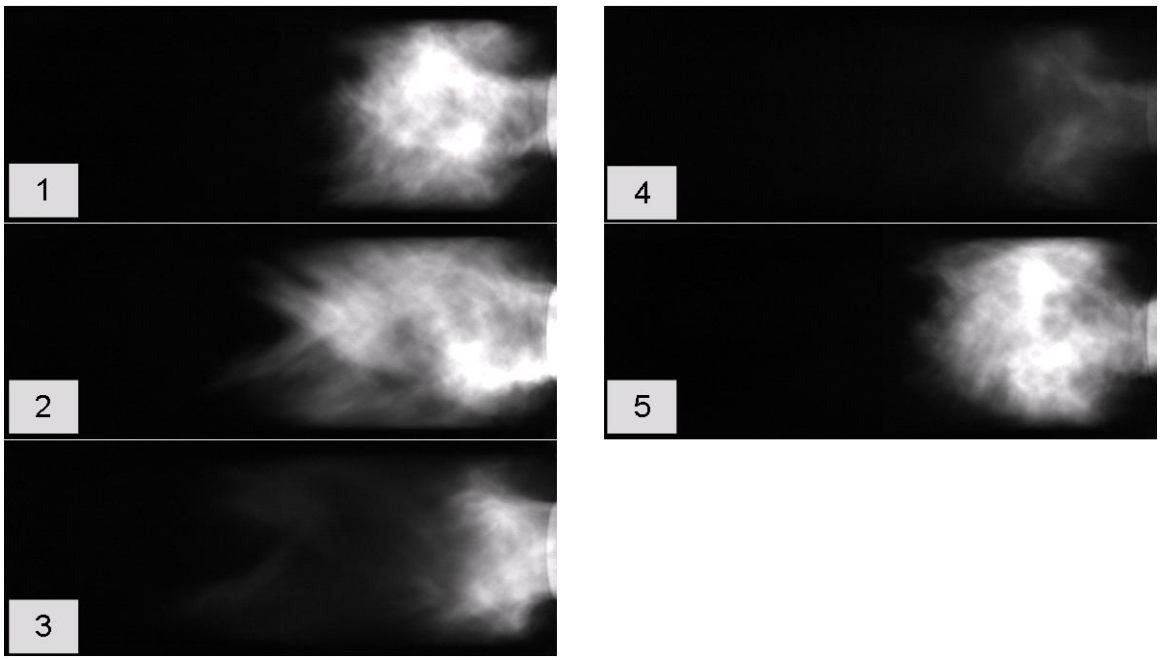

Figure 4-2: Sequence of images in a cycle during the five-quarter wave mode for $CH_4/O_2/CO_2$ flames with $X_{CO_2} = 0.594$ ($T_{ad} = 2200$ K) at $Re = 20{,}000$. Images are 2ms apart.

flame switches to a columnar type, similar to the ones reported by Zhang et al. [35] and Muruganandam et al. [25]. No instability is observed in the frequency-spectra for these cases.

So far the results have been plotted as a function of X_{CO_2}, corresponding to adiabatic flame temperatures in the 1700-2200 K range. Now, consider the flame speeds for these mixtures: If the dilution is adjusted to get $T_{ad} = 2050$K in a $CH_4/O_2/CO_2$ mixture (conditions matching Figure 4-3), the computed laminar burning velocity is 10 cm/s. For CH_4/air mixtures, this flame speed value is well below the flame speed at the laminar flammability limit, namely 15 cm/s. It is surprising then that a reasonably compact flame is observed for these conditions. However, turbulent mixing likely plays a critical role in maintaining the compact flame in oxy-combustion.

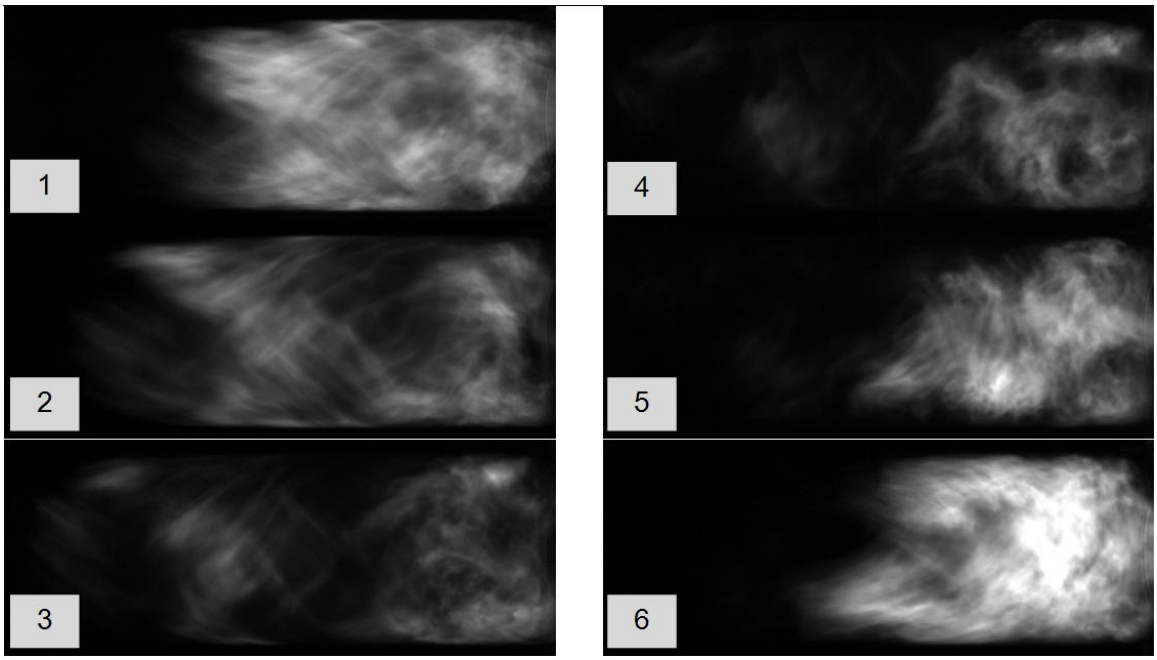

Figure 4-3: Sequence of images in a cycle during the three-quarter wave mode for $CH_4/O_2/CO_2$ flames with $X_{CO_2} = 0.659$ ($T_{ad} = 2000$ K) at $Re = 20{,}000$. Images are 2ms apart.

4.2 Comparisons with CH_4/Air Flames

OASPL curves similar to the one plotted in Figure 4-1 are plotted in Figure 4-5 for CH_4/air mixtures at the same Reynolds number, i.e. 20,000. The results indicate that the dynamic response of the combustor is essentially similar to that presented in Section 4.1 for oxy-fueled mixtures in two ways. First, as the adiabatic flame temperature is decreased (in this case by turning down the equivalence ratio), the instability modes transition from the five-quarter wave mode to three-quarter to the quarter wave mode before eventually blowing off.

The second similarity is in the overall turbulent flame structure. For this consider Figure 4-6 and Figure 4-7. The adiabatic flame temperature and Reynolds number for these cases have been adjusted to match the conditions in Figure 4-3 and Figure 4-4, respectively. Looking at these figures side by side, the visible turbulent flame shapes are very similar as are the underlying vortex breakdown modes. These results suggest that the underlying flow-field is a strong function of the temperature jump

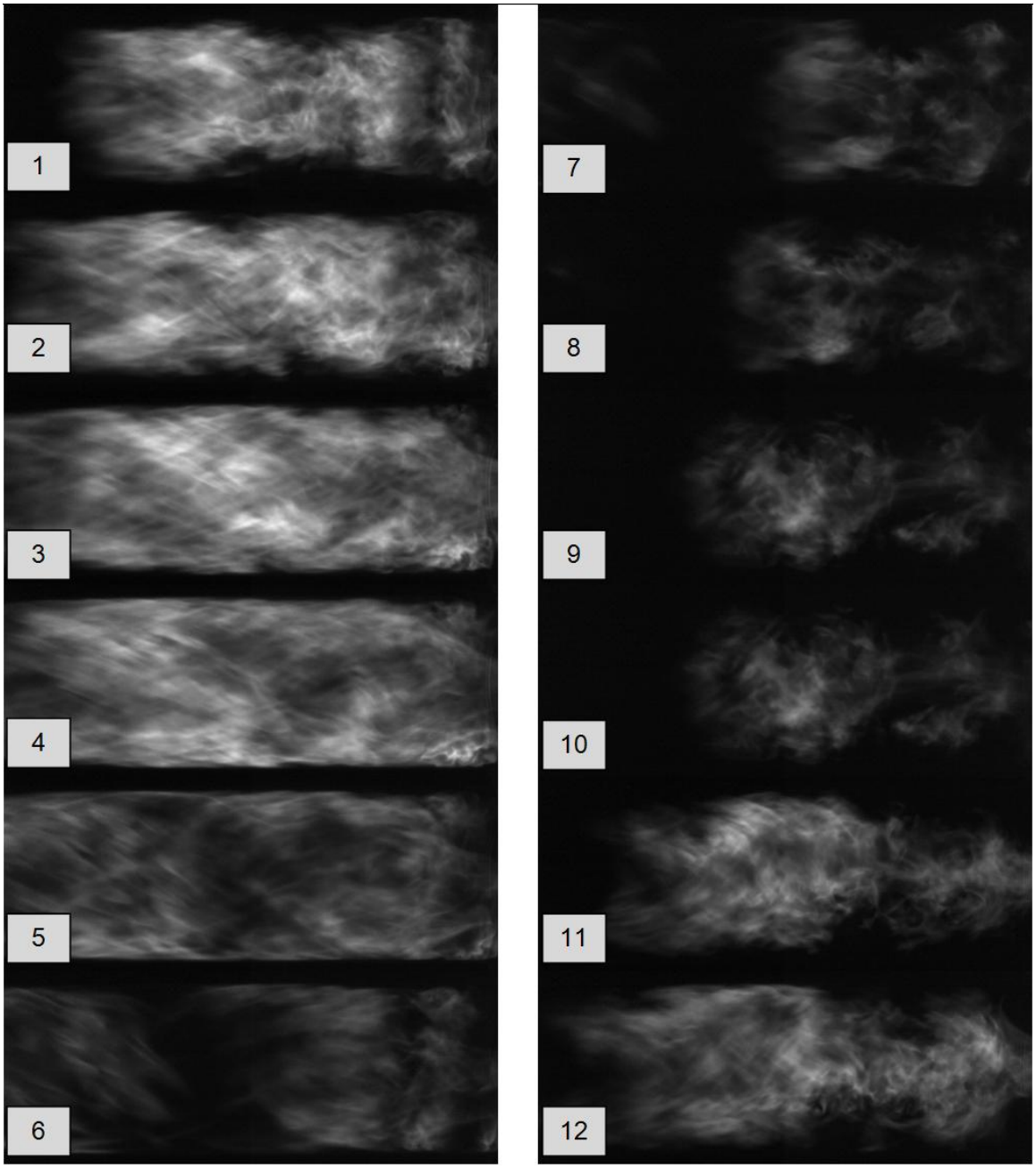

Figure 4-4: Sequence of images in a cycle during the quarter wave mode for $CH_4/O_2/CO_2$ flames with $X_{CO_2} = 0.686$ ($T_{ad} = 1900$ K) at $Re = 20{,}000$. Images are 2ms apart.

across the flame. Some subtle differences exist for instance, in Figure 4-7 (CH_4/air), a waist is seen between the bubble upstream and the double-helix downstream. This structure is a bit weak in Figure 4-4a ($CH_4/O_2/CO_2$). Since the mass flow rates are nearly the same, differences in flame speed would lead the oxy-flame to bulge laterally to a larger volume to burn the same mass. Still, the mode transitions and flame geometries are clearly controlled by the flame temperature at a given Reynolds number, at least to the first order.

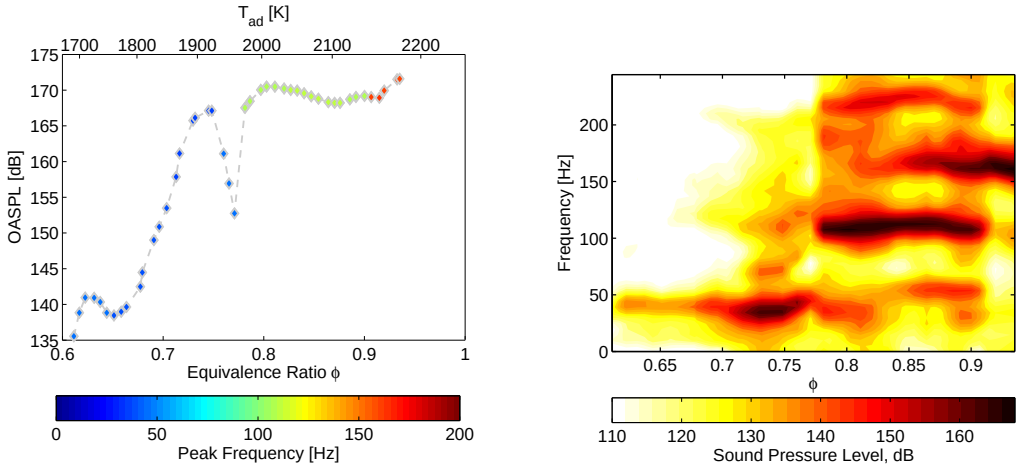

(a) OASPL for Re = 20,000

(b) Frequency spectrum for Re = 20,000

Figure 4-5: OASPL (a) and spectrum (b) of oscillations as a function of adiabatic flame temperature for CH_4/air mixtures at Re = 20,000. For reference, note the two x-axes in (a).

OASPL comparisons between air combustion, in which the equivalence ratio is varied, and stoichiometric oxy-combustion, in which the CO_2 mole fraction is varied, for constant Reynolds numbers from 15,000 to 30,000 are shown in Figure 4-8. The equivalence ratio is maintained at unity in all the oxy-combustion tests. Each curve represents one test sequence in the combustor from ignition at the high temperature end toward blowout at the lower end. Because the mixtures are varied in different ways between the air and oxy-combustion cases, the adiabatic flame temperature for the given mixture is used as the abscissa. Small gradients in color from point to point show mild frequency shifts (as the burnt gas temperature decreases w.r.t the reactants; this is expected, see Speth [12]).

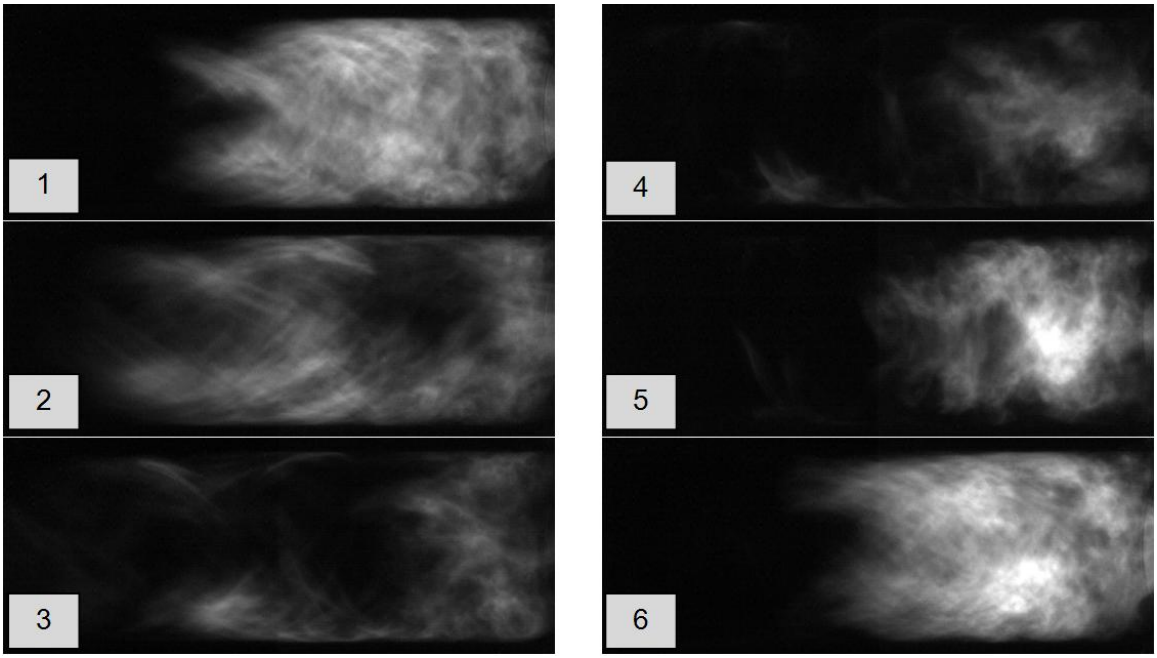

Figure 4-6: Sequence of images in a cycle during the three-quarter wave mode for CH_4/air flames with $\phi = 0.798$ ($T_{ad} = 2000$ K) at $Re = 20{,}000$. Images are 2ms apart.

While weaker flames are expected in oxy-combustion, because of the significant change in the consumption speed [36], surprisingly, similar dynamic modes and transitions seen in air combustion and oxy-combustion. With the exception of $Re = 30{,}000$, mode transitions collapse well when using the adiabatic flame temperature across the two combustion modes. At $Re = 25{,}000$, for instance, there is one clear transition at $T_{ad} = 2100$ K from the five-quarter mode to the three-quarter mode and another at $T_{ad} = 1950$ K from the three-quarter mode to the quarter-wave mode.

Strongest instabilities, those over 165 dB, exist at higher flame temperatures where a compact unstable flame exists in 3/4 or coexisting 3/4 and 5/4 wave modes. These peak frequencies are shown in Figure 4-9 that plot the frequency spectrum (truncated up to 250 Hz) as a function of the adiabatic flame temperature. The right and left edges of each plot are simply the condition at which data recording begins and the condition at blowout, respectively, so there is variation between plots. In oxy-combustion, the dominant frequencies for the high, medium, and low frequency modes are in the ranges of 125-150 Hz, 80-100 Hz, and 25-40 Hz, respectively. Frequencies

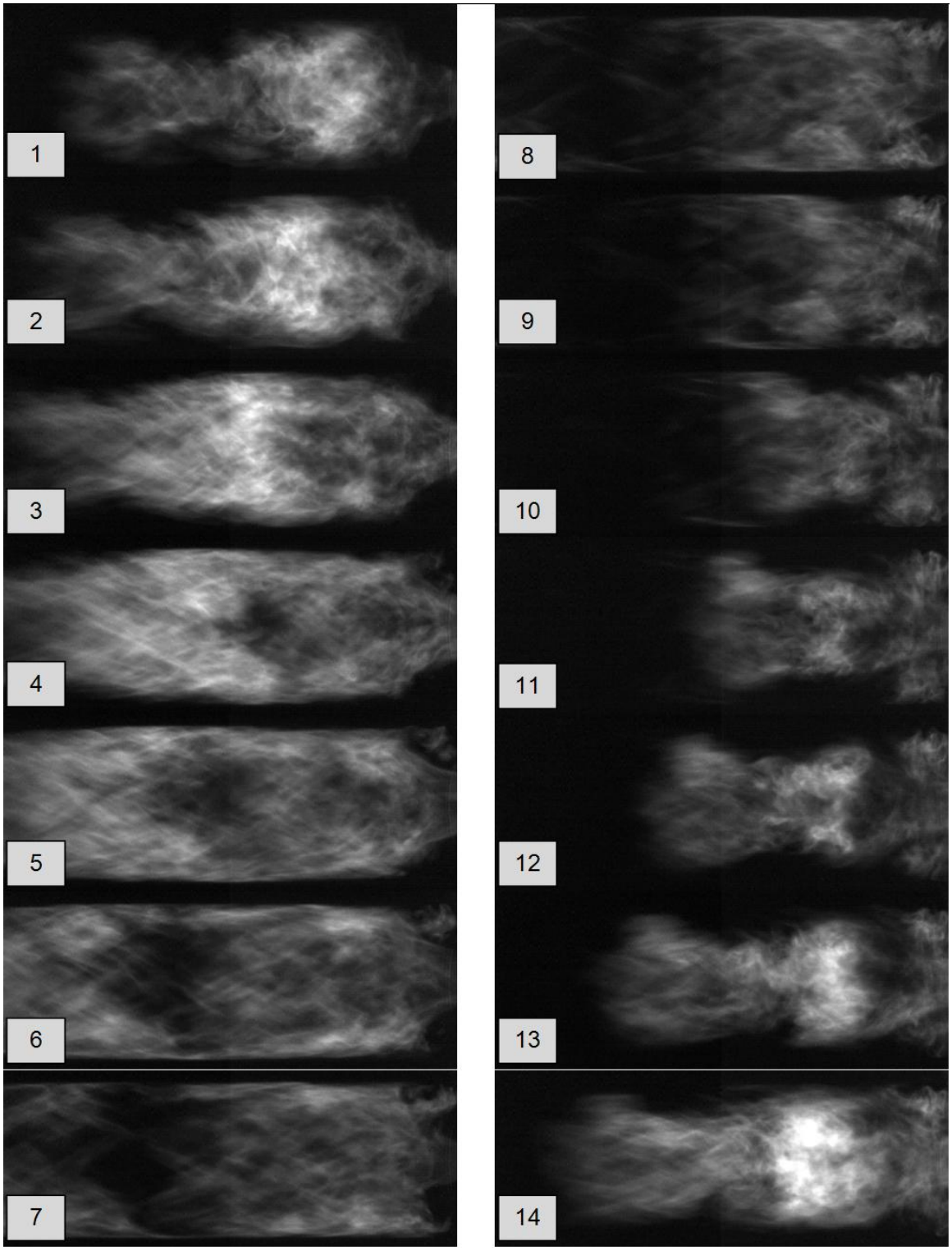

Figure 4-7: Sequence of images in a cycle during the quarter wave mode for CH_4/air flames with $\phi = 0.734$ ($T_{ad} = 2000$ K) at $Re = 20{,}000$. Images are 2ms apart.

for the three modes are shifted higher for air to 150-170 Hz, 100-120 Hz, and 30-50 Hz. The shift, as discussed in Section 4.3, is due to the differences in acoustic properties of the products and reactants between air and oxy-combustion. While the quarter wave mode exists alone in all cases, the three-quarter and five-quarter wave modes coexist in an overlap region. The five-quarter wave mode is dominant at the highest temperatures. The temperature range where modes coexist diminishes with increasing Reynolds number.

As the flame temperature is decreased by changing the mixture composition, transitions occur to lower harmonics. In some cases, namely air combustion at all Reynolds numbers except for 15000, a hole exists (e.g. between T_{ad} = 1930 K and 1980 K for Re = 20,000) in this transition where the flame is considerably more stable. The sound pressure levels for these conditions are much lower for air flames compared to oxy-flames. The reason for this is not entirely clear, but is a subject of future investigation.

Regardless of whether the fuel is burned in air or in O_2/CO_2, the low frequency (quarter-wave) unstable flames are several times longer than the compact unstable flame. A stable columnar flame that extends well into the exhaust is seen at the lowest temperatures for all Reynolds numbers before blowoff where the OASPL drops off significantly.

4.3 Frequency Ratio

The limit cycle frequencies corresponding to the previous figures are shown in Figure 4-10. The lowest frequencies correspond to the 1/4 wave mode, and the 3/4 wave mode is shown by the middle grouping. The 5/4 wave mode also exists as a dominant mode at high temperatures for all cases except oxy-combustion at Re = 30,000 and air combustion at Re = 15,000 (for these two cases, the 5/4 wave mode can be seen as co-existing in Figure 4-9). It is expected that if the combustor was completely adiabatic, the limit cycle frequency would be relatively insensitive to the Reynolds number. This expectation comes from compact flame acoustic models, where the

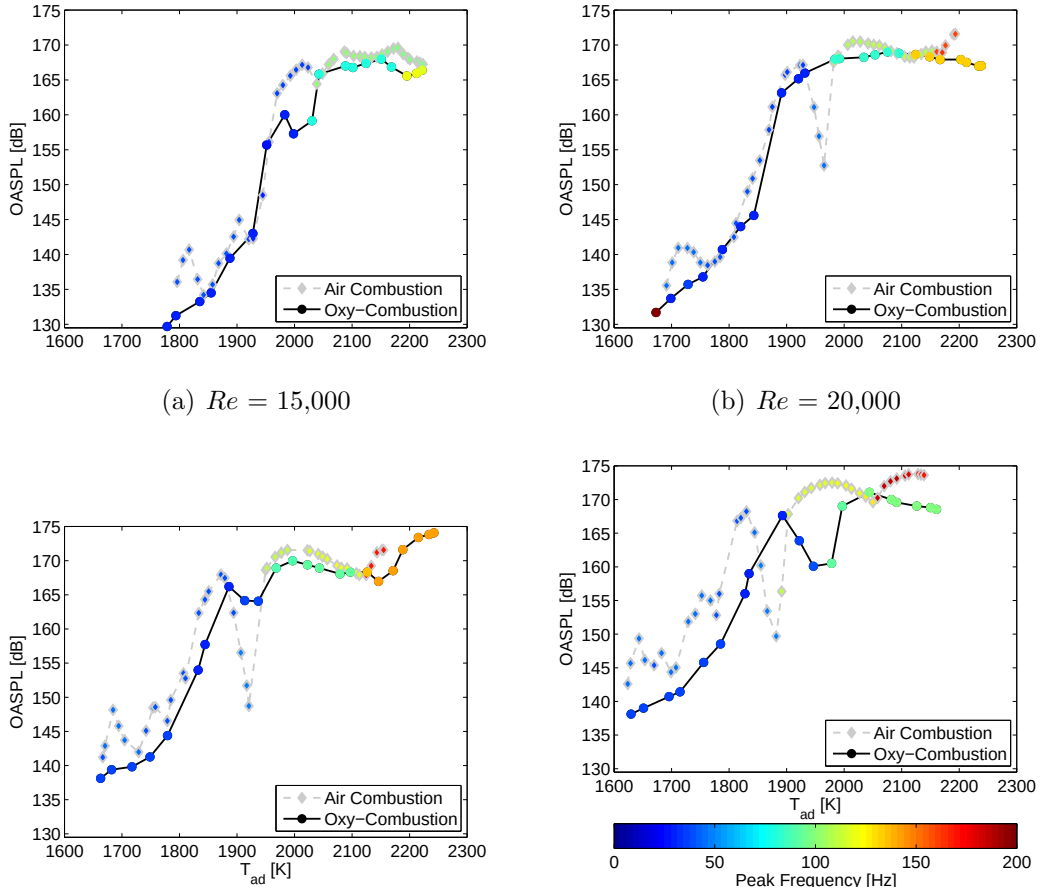

(a) Re = 15,000 (b) Re = 20,000

(c) Re = 25,000 (d) Re = 30,000

Figure 4-8: OASPL comparison as a function of adiabatic flame temperature for Re = 15,000 to 30,000.

length of the flame L_f is much less than the acoustic wavelength λ, i.e. $L_f/\lambda \ll 1$. For the cases shown, the worst case is approximately $L_f/\lambda = 0.1$. In actuality, the frequency climbs with Re. Speculations for the cause include heat loss affecting the acoustic properties or the effect of Re on flow structure. If the flow structure is affected, a change in the coupling of heat release, flow, and acoustics could cause the frequency shift. The frequency for oxy-combustion is always lower, and the ratio for each mode and Reynolds number are summarized in Table 4.1. Using Equation (10) from Altay et al. [1], the expected resonant frequencies are plotted against T_{ad} in Figure 4-11. These curves match the experiments fairly well. Note, however, that the equation does not predict which mode will exist at each temperature, so the curves span the entire operating range. The predicted frequency ratios (f_{OXY}/f_{AIR}) are

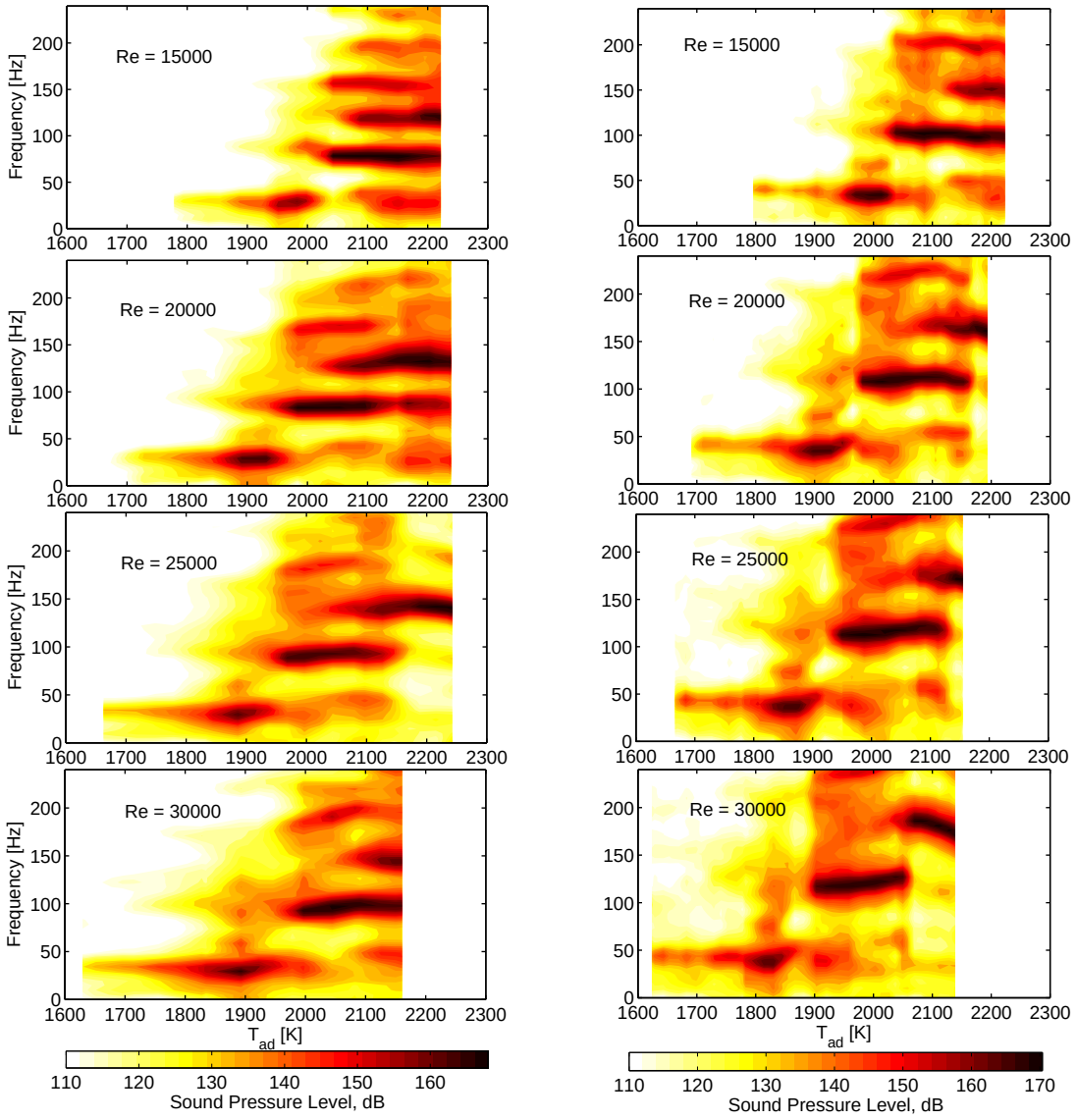

(a) Oxy-combustion

(b) Air combustion

Figure 4-9: Frequency maps for air and oxy-combustion for Re = 15,000 to 30,000.

shown in Figure 4-12. These three ratio curves lie within the envelope created by the speed of sound ratio (c_{OXY}/c_{AIR}), where the speed of sound $c = \sqrt{\gamma RT}$ (assuming an ideal gas mixture) is dependent on the mixture specific heat ratio γ and the gas constant R. The upper bound is created by using only unburned mixture properties and the lower bound by using only burned mixture properties. Based on the average experimental ratio of 0.8 from Table 4.1, it can be concluded that, at least to first order, the change in dynamic frequency from air to oxy-combustion is explained by

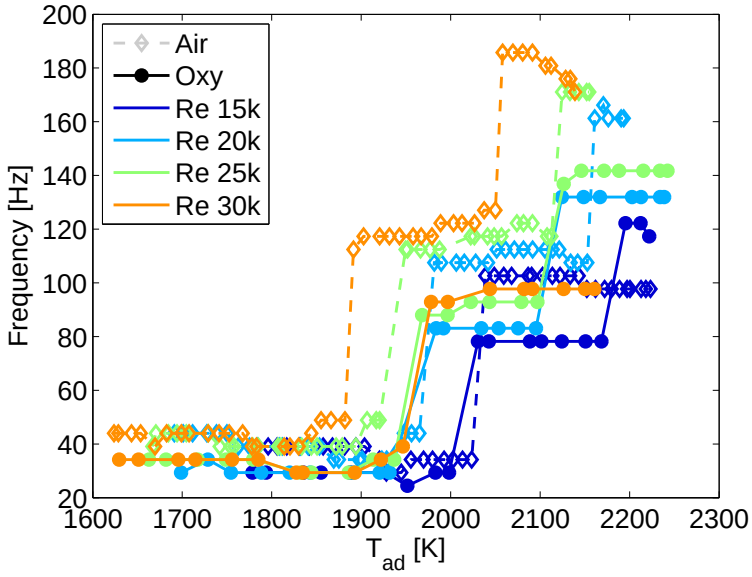

Figure 4-10: Experimental frequencies.

acoustic properties of the mixtures.

Table 4.1: Ratio of experimental frequencies (oxy/air) for each wave mode.

Re	1/4 wave mode	3/4 wave mode	5/4 wave mode
15,000	0.86	0.76	
20,000	0.75	0.77	0.82
25,000	0.88	0.79	0.83
30,000	0.78	0.80	

4.4 Hysteresis in Mode Transition

For all the cases presented so far, the experiments were conducted by igniting the mixture at high equivalence ratios or high O_2 fraction and then gradually lowering it until blowoff. Results collected in this case indicate that there are two distinct transitions: a transition from the 3/4 to 1/4 wave mode at high temperatures, and another from the 1/4 wave mode to stable case at lower temperatures close to blowoff.

Now, consider results from experiments conducted in the reverse order by increasing the equivalence ratio or O_2 concentration (and hence the temperature) gradually

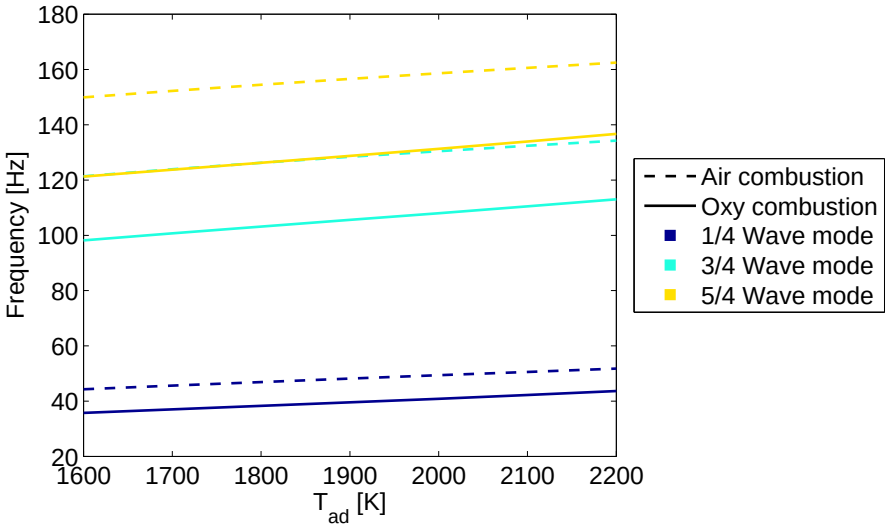

Figure 4-11: Predicted frequencies as a function of adiabatic flame temperature for the three modes seen experimentally.

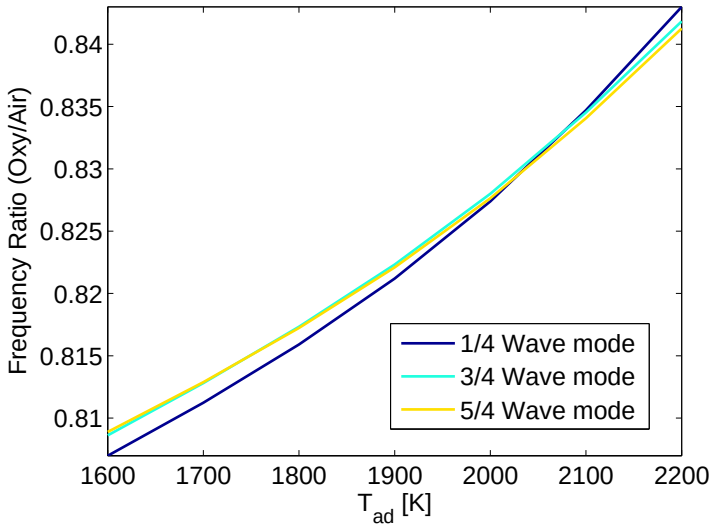

Figure 4-12: Predicted frequency ratios comparing air and oxy-combustion for the three modes seen experimentally.

until high temperatures are reached. These data are illustrated in Figure 4-13(a) for air and Figure 4-13(b) for oxy-fuel mixtures. This figure shows that the instability at the 1/4 wave mode persists for much higher flame temperatures before transitioning to the 3/4 wave mode, if the experiments are conducted by increasing the adiabatic flame temperature.

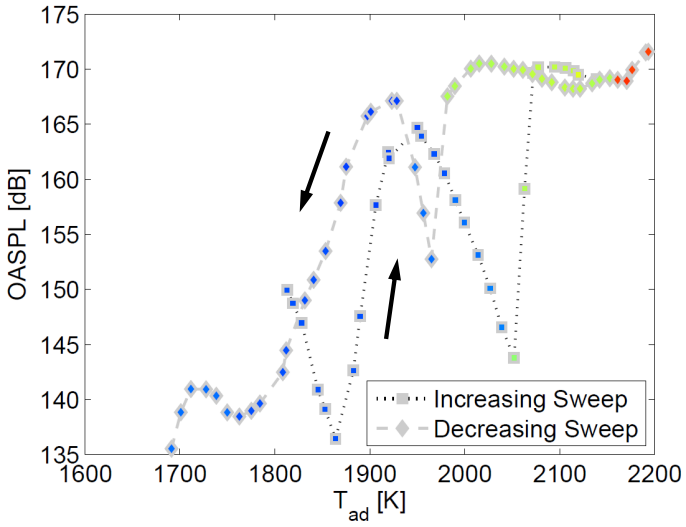

(a) Air combustion

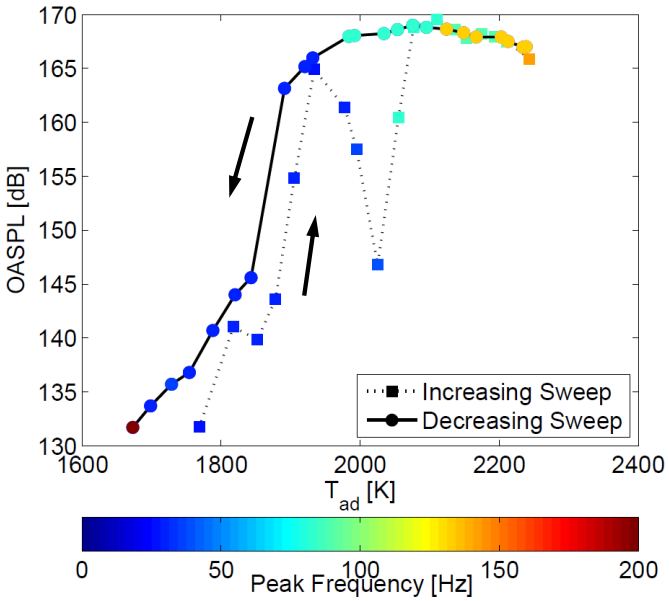

(b) Oxy-combustion

Figure 4-13: Hysteresis shown by comparing increasing and decreasing sweeps at Re = 20k.

These data suggest that mode transition depends on whether the combustor load-

ing is increased or decreased, that is, it depends on the state and the history. At this point the interest is in determining whether the transitions depend on the temperature pathway or are function of the pathway followed by some other state variable. For this purpose, another experiment was conducted; this time the combustor was ignited and immediately switched to $T_{ad} = 2030$ K. According to Figure 4-5, at this point the combustor should be in the 3/4 wave mode as per the decreasing temperature path; but just at the border of the transition between the 1/4 to 3/4 wave mode as per the increasing temperature path. Once ignited the equivalence ratio was then gradually decreased. The trajectory of the limit cycle amplitude as a function of the temperature is illustrated in Figure 4-14. The figure shows that despite the decreasing temperature, the trajectory followed by the amplitude overlaps with the trajectory obtained as if the temperature was increased. This proves that the hysteresis in mode transitions is not just a function of temperature (and thus independent of the types of mixtures being burned). An area of future tests is to identify a state variable that controls the hysteresis, but so far the data suggests that this is dependent on the instability frequency the combustor is in just prior to the point when the temperature is increased or decreased.

One should also note that the trajectories (and consequently the blowoff limits) deviate below $T_{ad} = 1940$ K. This is in turn due to the hysteresis of the 1/4 wave mode with respect to the stable mode. Stated differently, if the combustor is ignited and suddenly brought to $T_{ad} = 1810$K, the combustor is observed to be stable. The temperature has to be increased to $T_{ad} = 1890$K to kick it into the 1/4 wave mode. However if the combustor is brought to $T_{ad} = 1890$K slowly from higher temperatures when the 1/4 wave mode is present, the same mode persists until lower temperatures.

Considering the effects of the hysteresis, the data that was presented throughout this document was recorded by increasing the flame temperature after ignition until the combustor is kicked into the five-quarter mode, and then decreasing the temperature gradually. For CH_4/Air mixtures, one could argue that this is guaranteed by always starting at stoichiometric conditions and then decreasing the temperature. However, for $CH_4/O_2/CO_2$ mixtures, the maximum temperature that can be attained

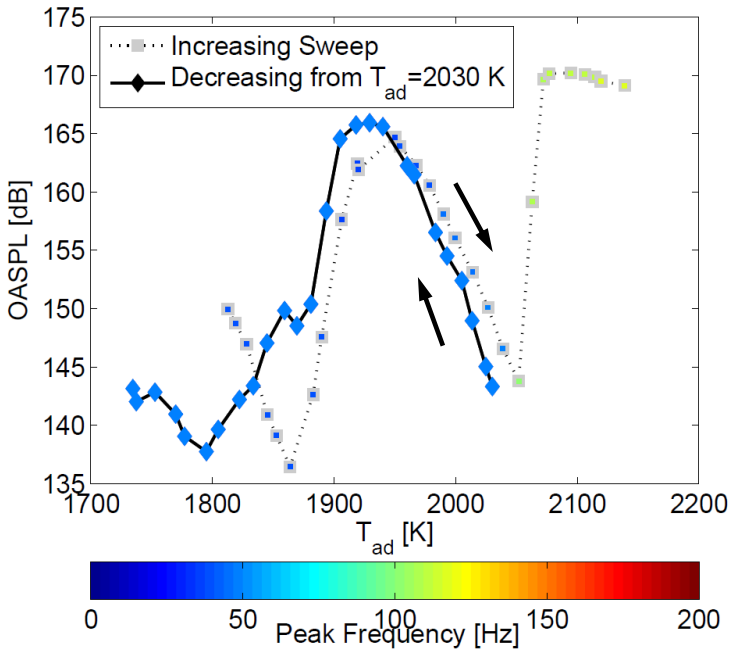

Figure 4-14: Mode history dependence for air combustion at Re = 20,000. For the decreasing sweep, the test was conducted by igniting the flame at T_{ad} = 2030 K and then decreasing gradually.

is T_{ad} = 3051K; but this was not possible given the temperature limitations of this combustor. Hence the amount of dilution in the flow was reduced just enough to trigger the five-quarter wave mode.

Finally, for both air and oxy-combustion, the shift in transition temperature between the 1/4 and 3/4 from hysteresis is on the order of 50 K. However, the quiet transition region between the 1/4 and 3/4 unstable modes is extended for air combustion and introduced for oxy-combustion. That is, a significantly more stable flame can be achieved at 2000 K for oxy-combustion by approaching the corresponding mixture composition while in the low frequency mode. As a result, the space of operation where the sound pressure level is over 165 dB is significantly decreased for the increasing sweeps. Making use of phenomena such as this could be exploited as an operation strategy for gas turbines.

4.5 Dynamics Conclusions

In this chapter the combustion dynamics characteristics of $CH_4/O_2/CO_2$ mixtures and CH_4/Air mixtures are compared in a swirl stabilized combustor. Although weaker flames are expected in oxy-combustion due to lower consumption speed, the flame structures of air and O_2/CO_2 flames in each of the modes are similar. The transitions from one instability mode to another are shown to be a function of the mixture adiabatic flame temperature for $Re \leq 25{,}000$. The data match less well for $Re = 30{,}000$; the reasons for this could include heat transfer effects in the non-adiabatic combustor. Additional strained flame calculations with an asymmetric configuration having products on one side (unlike the twin flame configuration in Chapter 3) could potentially provide more relevant values for S_c that explain combustor behavior. The data also reveal hysteresis with respect to mode transitions, which are shown to be mode-dependent and not temperature dependent. This fact could be exploited for developing control strategies to avoid a particular mode of instability. Another important note that increases the significance of flow structure and its complexity is that the range of Reynolds numbers from 15,000 to 35,000 used in this chapter and Chapter 5 are likely in the transition to turbulence range. That is, the flow is not yet fully developed because large scale structures in the vortex breakdown of the swirling flow are a function of Re. Therefore, the combustor behavior should be less dependent on Re above some critical Reynolds number.

Chapter 5

Blowoff

This chapter explores the experimental results using the open exhaust configuration as shown in Figure 2-4(b). The flame still resides in the quartz tube, but the acoustics of this configuration are such that thermo-acoustic instabilities to not occur, except at temperatures above those presented here. As such, transport properties, etc., drive the behavior of the system in a more significant way than the cases in Chapter 4 where heat release rate is a driving factor. Both static stability (blowoff) and higher temperature flow and flame structures are presented. Experiments using PIV are all at 1000 Hz and $Re = 20{,}000$. PIV results are averaged over approximately 0.5 seconds of data.

Currently, several approaches to blowoff phenomena exist, as summarized by Shanbhogue et al. [29]. Also, recent state-of-the-art advances in PIV and PLIF systems have allowed researchers to push closer to detailed, high-speed images of local flow and flame information. While this thesis provides only introductory information on oxy-combustion blowoff trends, continued work with imaging techniques have the potential to advance the field significantly toward a unified theory. For example, Chaudhuri et al. [4] used simultaneous PIV and OH PLIF on an axi-symmetric bluff body flame and demonstrated the importance of stretch rates in shear layers on extinction. One example of blowoff research in a swirl-dump-stabilized combustor is by Muruganandam and Seitzman [25], who took chemiluminescence images and concluded that packets of reactants entering the inner recirculation zone overwhelm

the flame with local extinction and lead to blowoff.

5.1 Flame Modes and Blowoff

The flame structure in the combustor exists in several modes which depend on temperature. For each Reynolds number, tests are performed beginning at a high temperature and decreasing the temperature by increasing X_{CO_2} in oxy-combustion (at $\phi = 1$) or decreasing ϕ in air combustion. Example photographs of each mode are shown in Figure 5-1. At the highest temperatures tested, the flame structure exists in its most compact form as a 'tulip' shaped mode that includes a flame in the outer recirculation zone (ORZ). As the temperature is decreased slowly in small, discreet increments, the flame in the outer recirculation zone suddenly disappears, leaving a tulip shaped mode that is somewhat longer. Intermittently, there may still be a brief flash of flame in the ORZ for a small temperature range. The next sudden transition in flame structure coincides with a dramatic change in flow structure. In this transition, the flame jumps from the tulip mode to an axi-symmetric bubble mode, and flow structure changes are shown in Section 5.2. The final transition before blowoff is a gradual transition from the axi-symmetric bubble mode to a spiral flame mode. In this transition, the bubble weakens before finally disappearing. This weakening is shown in parts 4 and 5 of Figure 5-1. Not shown in this figure is the state of the flame just before blowoff, where the flame is no longer anchored in the proximity of the dump plane but instead moves downstream along the axis of the quartz tube. The upstream-most portion of the flame tends to move back and forth along this axis unsteadily. Hence, the actual point of blowoff has variance between runs.

The summary of these mode transitions is shown in Figure 5-2. These data points are taken by hand from visual inspection of the flame. Some of these data points are averaged over a number of runs, while some are taken from single values. The transition temperatures for air and oxy-combustion do not line up like the temperatures for dynamic instability modes in Chapter 4, and the suspicion is that transport properties play more of a fundamental role in this configuration where thermoacoustic instabil-

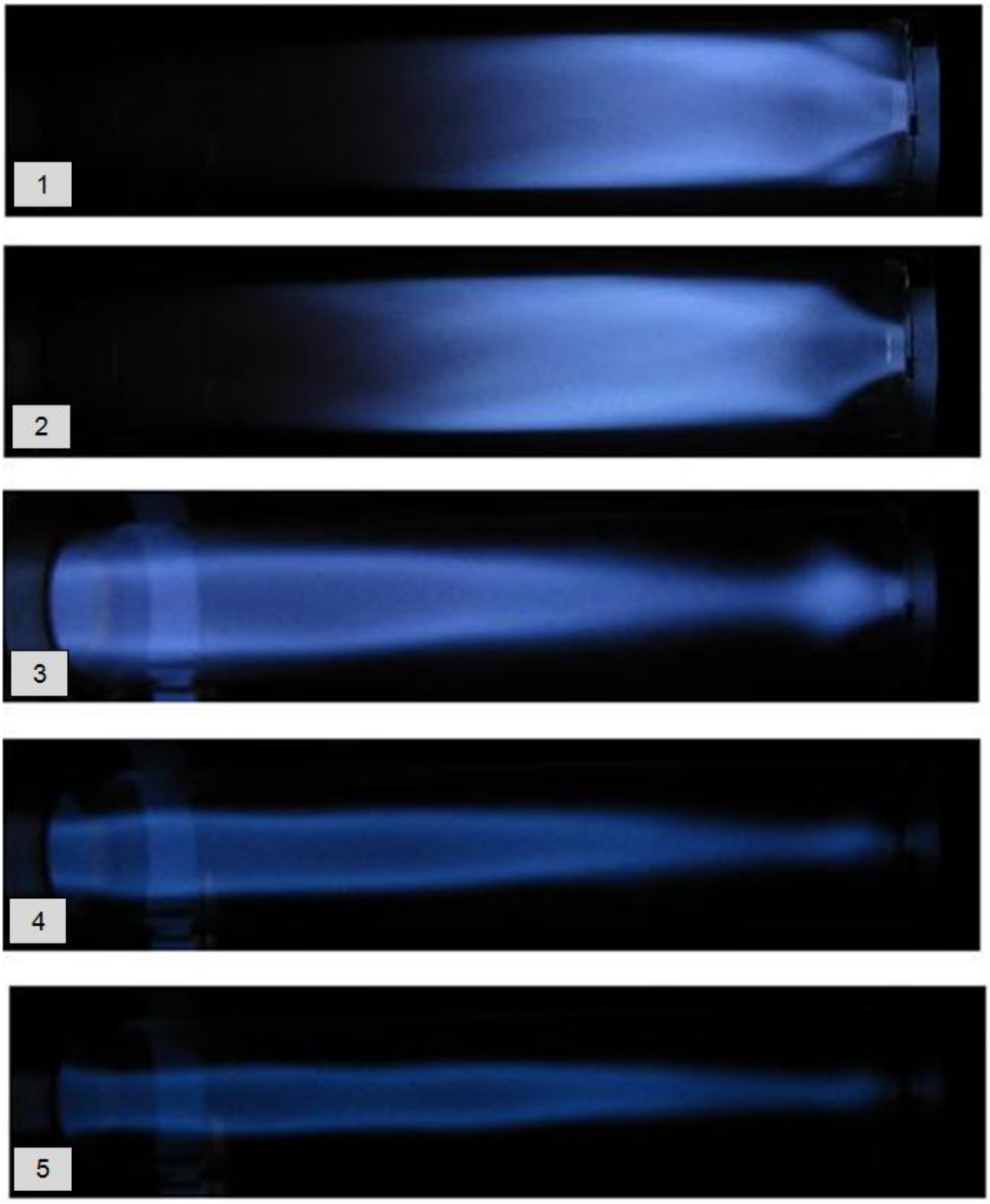

Figure 5-1: Oxy-combustion pictures taken with a Canon PowerShot SD780 from (1) most compact flame with ORZ downward in temperature through (2) without flame in ORZ and (3) axi-symmetric bubble to (4,5) gradually weakening spiral mode. Flow is from right to left. The conditions correspond to temperature ranges within the four upper zones of a vertical slice of Figure 5-2(a) at Re = 32,500: (1) >1930 K, (2) 1930 K to 1860 K, (3) 1860 K to 1820 K, (4,5) 1820 K to 1730 K.

ities are not present. Overall trends, however, are similar, with the temperature of transition generally decreasing with increasing Reynolds number. It becomes apparent that this is actually the opposite trend of what one might expect when looking at the blowoff curves. At higher temperature, one would expect that a higher velocity could be sustained as shown by Zukoski [37]. The exception to this unexpected trend is oxy-combustion at Reynolds numbers from 25,000 to 35,000.

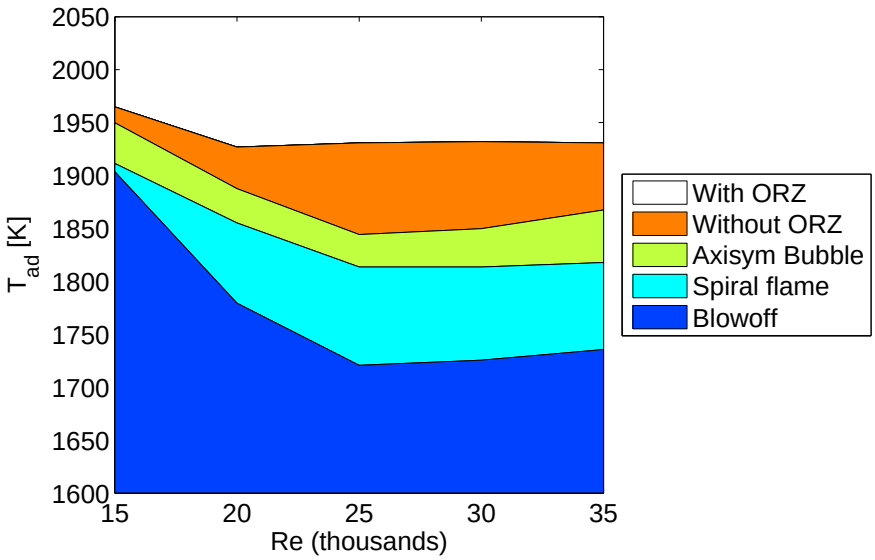

(a) Oxy-Combustion

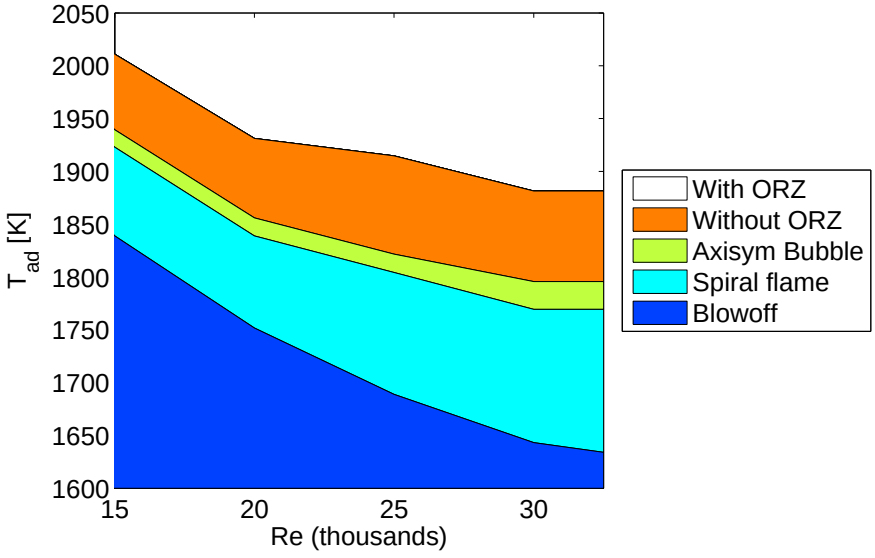

(b) Air Combustion

Figure 5-2: Flame mode maps for (a) oxy-combustion and (b) air combustion.

Blowoff results (same as the bottom transition curves in Figure 5-2) are summarized in Figure 5-3. The velocity used is the mean inlet velocity at blowoff, v_b. As expected, oxy-combustion flames blow off at a higher temperature for a given Reynolds number due to weaker flames. The unexpected negative slope, however, is similar to those seen in the oxy-combustion studies of Amato et al. [2]. In that work, the negative slope is only seen in the middle section of an S-shaped curve of blowoff velocity vs temperature. This suggests that perhaps for their geometry this is a transition to turbulence region. This could also be the case for the combustor used in this thesis, but flow range limitations presented here prevent testing at higher or lower Reynolds numbers than those presented. For oxy-combustion at Reynolds numbers from 25,000 to 35,000, however, the curve knees upward to the expected positive slope, suggesting that there is a change in the flame speed and/or mixing relative to the local flow field that supports higher velocities at higher temperatures.

Interestingly, the suggestion of Zabetakis [34] that the ratio of flammability limits for mixtures with different diluents is approximately inversely proportional to the burned gas heat capacities can be used to collapse the air and oxy-combustion blowoff curves. Shown in Figure 5-4 is v_b times the heat capacity at blowoff vs power at blowoff, where the power is simply the fuel mass flow rate times the lower heating value (LHV) of the fuel. This collapse shows that the blowoff velocity appears inversely proportional to the molar heat capacities of the burned gas mixtures at a given power, i.e. $v_{b,OXY}/v_{b,AIR} = \overline{c}_{p,AIR}/\overline{c}_{p,OXY}$. Note that the knee in the oxy-combustion curve in Figure 5-3 surfaces here as only a small change in slope. The slope of the air combustion blowoff data on the plot of mean inlet velocity vs power (recall Figure 2-5) corresponds to an adiabatic flame temperature of 1460 K ($\phi = 0.49$), which is approximately the equivalence ratio at the lean flammability limit for methane ($\phi = 0.5$). The oxy-combustion blowoff slope corresponds to $T_{ad} = 1620$ K, reinforcing the notion of weaker chemistry for oxy-combustion.

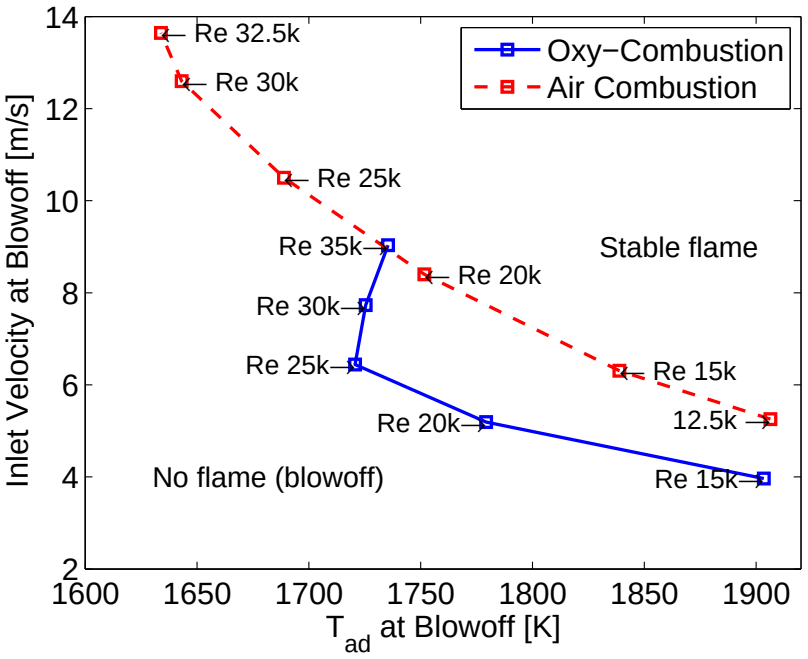

Figure 5-3: Blowoff velocity for air and oxy-combustion.

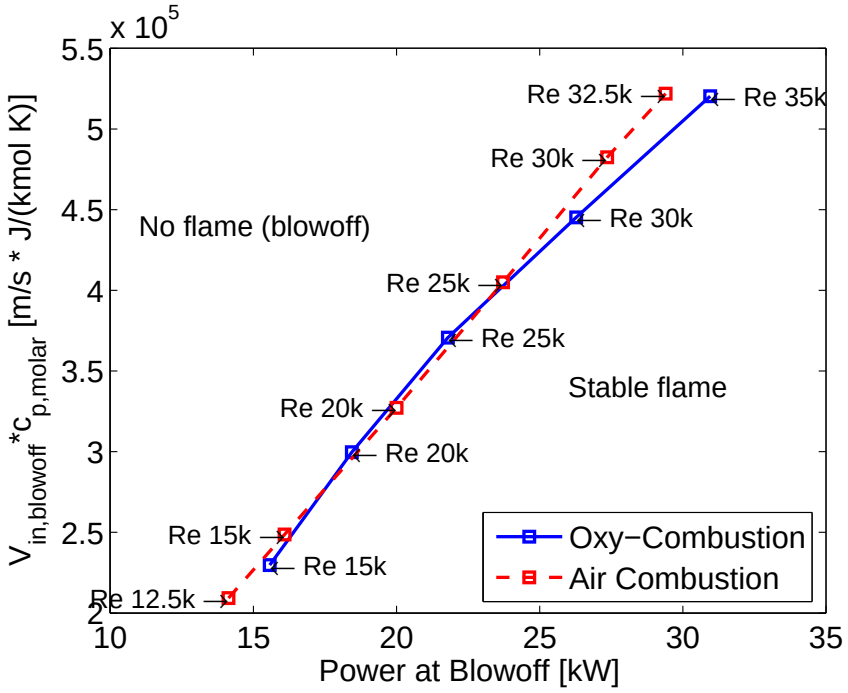

Figure 5-4: Collapse of air and oxy-combustion blowoff curves by plotting the mean inlet velocity at blowoff times the molar heat capacity of the burned gas mixture vs the thermal power at blowoff.

5.2 Flow Fields from PIV

The average flow structure for the two combustion types match very closely at $T_{ad} =$ 2060 K as shown in Figure 5-5. Both types have a strong downstream flow surrounding a relatively small teardrop-shaped inner recirculation zone (IRZ). Shown in Figure 5-6(a) are selected velocity profiles corresponding to Figure 5-5. The profile shapes are similar, but the magnitude of the velocity for air combustion is larger as expected from the higher mean inlet velocity at the same Reynolds number. When normalized, however, the profiles line up remarkably well.

At $T_{ad} = 1960$ K, the shape of the IRZ changes significantly, and now has a central core of downstream flow, as shown in Figure 5-7. Corresponding samples of instantaneous data in Figure 5-8 show unsteadiness in both the higher velocity inlet flow and the downstream flow field. At $T_{ad} = 1890$ K, air combustion maintains the same structure, but the flow structure in oxy-combustion has shifted to a spear-head shaped IRZ. This spear-head shape is not seen for air combustion until $T_{ad} = 1850$ K, as shown in Figure 5-12(a). The differences in velocity profiles are shown in Figure 5-10, where the normalized velocity in the outer (downstream velocity) portion of the flow still matches well, but the central flow (IRZ) shape is different. The gradual weakening of the bubble mode and transition to the spiral mode are shown in Figure 5-12 for air combustion. Instantaneous flow fields from Figure 5-12(d) are shown in Figure 5-13. This figure provides a sample of the evolution of unsteady structures near blowoff. Possibly due to changing the igniter configuration from the one used in Section 5.1 or variation in the flow from seeding, it was difficult to keep the flame lit in the spiral mode for oxy-combustion. Therefore, the lowest temperature presented for oxy-combustion is $T_{ad} = 1860$ K in Figure 5-11(b), which should correspond to the weakening axisymmetric bubble. The flow profiles matching well at high temperatures and less well at lower temperatures suggests that at high temperatures, the flow fields match up well due to required flame areas that are not drastically different (recall Figure 3-7).

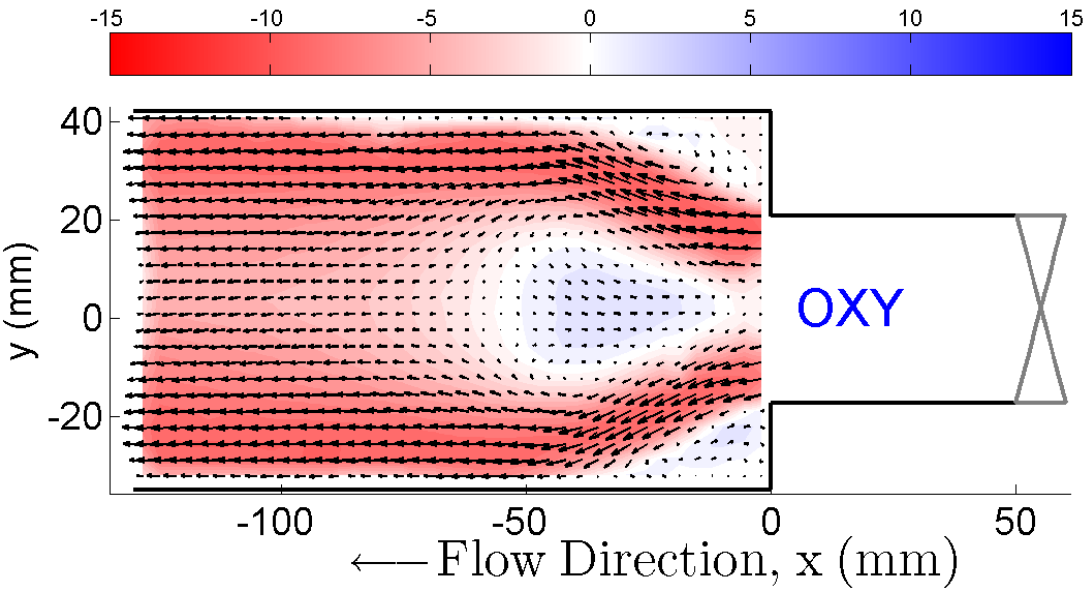

(a) Oxy at 2060 K

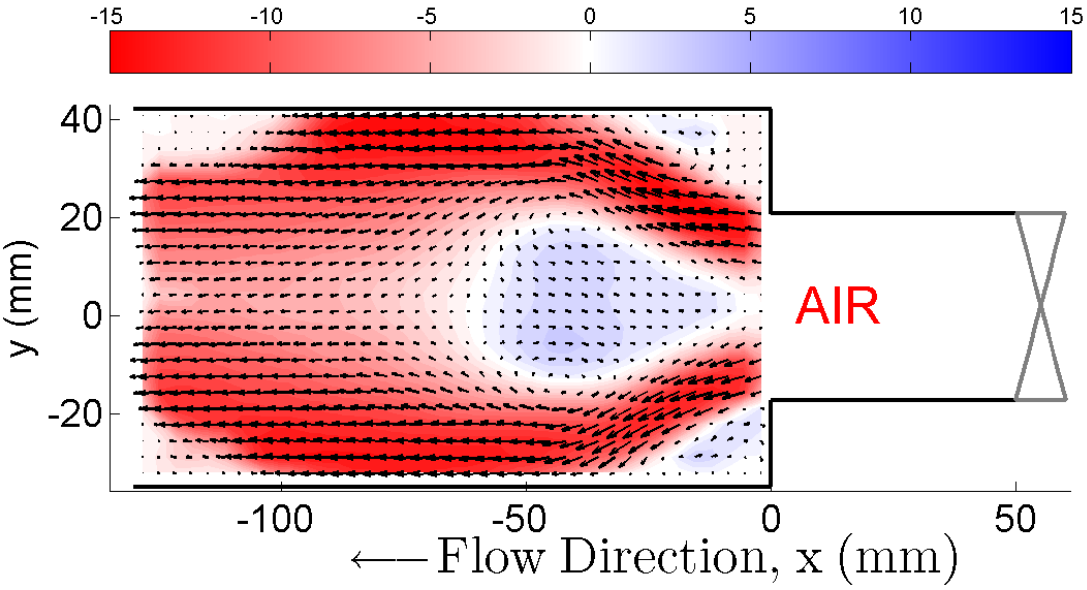

(b) Air at 2060 K

Figure 5-5: Flow field comparisons with a flame in the outer recirculation zone at T_{ad} = 2060 K and Re = 20,000. Colorbar units of x-component velocity are m/s.

5.3 PIV Challenges

High speed PIV with combustion is a challenge for a number of reasons, such as seeding particle build-up on the quartz tube and laser reflections. Geometry, however, is a factor that is crucial to both PIV and consistent results in combustion experiments.

If the flow is expected to be axi-symmetric because the geometry is supposed to be axi-symmetric, the experimentalist must be wary of the effects of measurement ports, etc., on the flow field. An example of strong asymmetry is shown in Figure 5-14(a) for cold flow at $Re = 20{,}000$. The cause of the asymmetry was found to be the position of the igniters (automotive spark plugs), located just downstream of the swirler. The tips of the plugs were protruding approximately 1 cm into the flow field, and the two opposed igniters were also rotated 30° from the image normal direction. Once the tips were recessed radially outward so they were no longer in the flow path, a much better result was achieved as shown in Figure 5-14(b). However, the presence of a precessing vortex core for this cold flow case is evidenced by the stronger downstream flow section switching from the top to the bottom of the field of view when repeating the test.

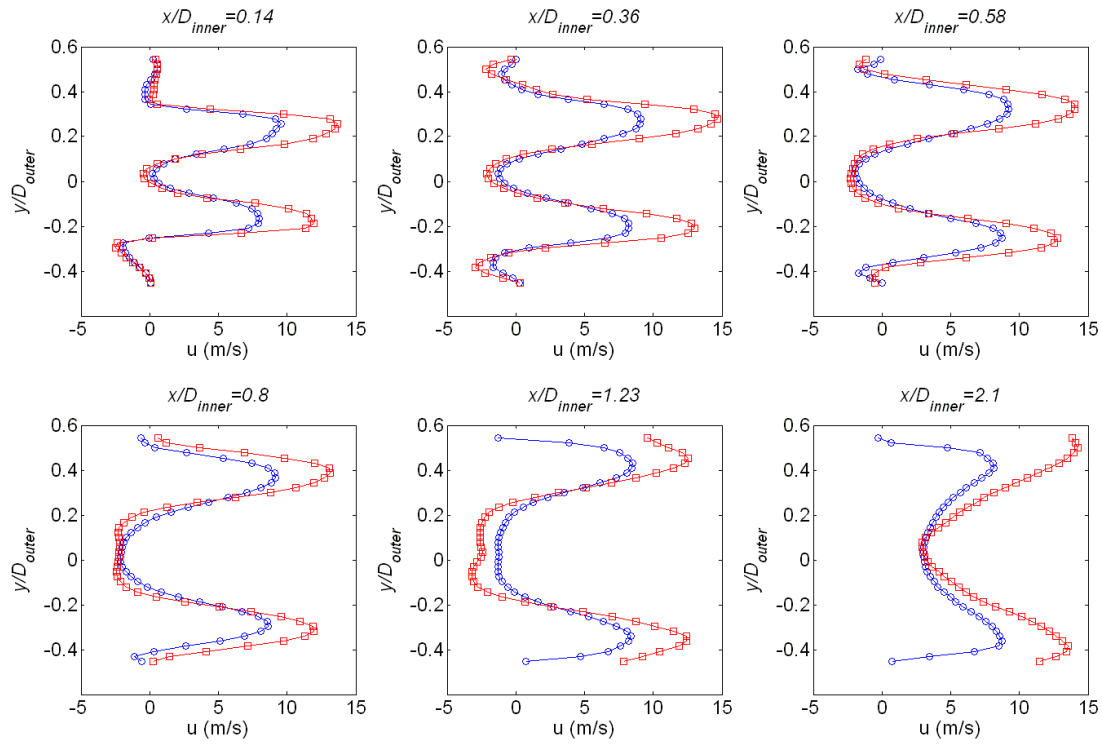

(a) Not normalized

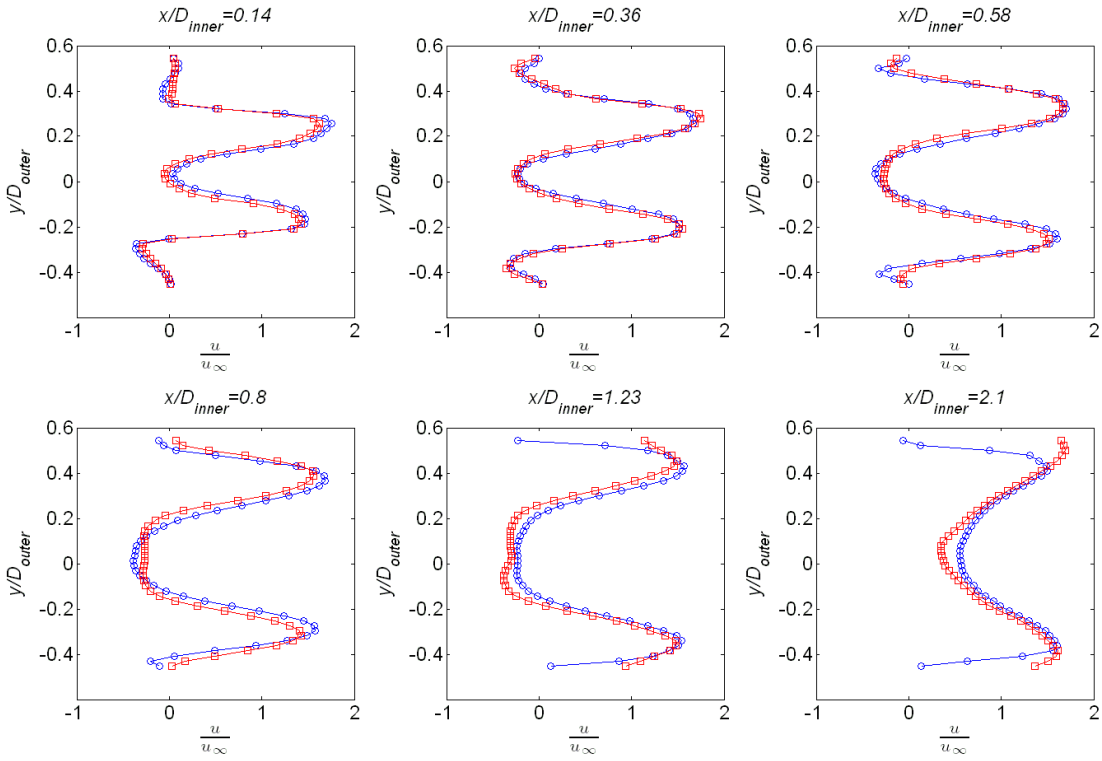

(b) Normalized

Figure 5-6: Velocity profile comparisons at T_{ad} = 2060 K and Re = 20,000. Blue circles are oxy-combustion and red squares are air combustion.

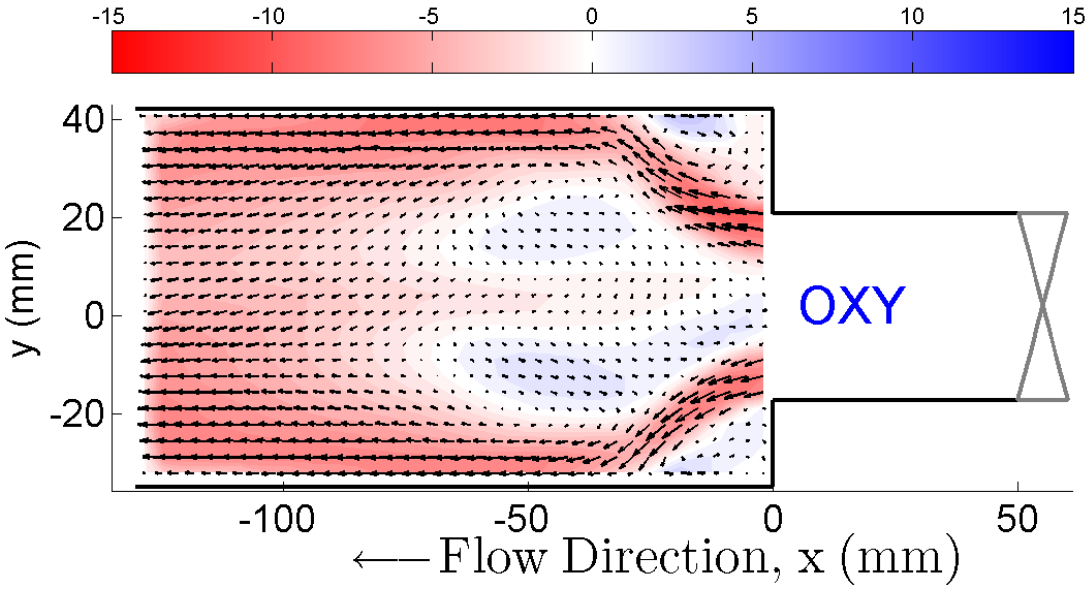

(a) Oxy at 1960 K

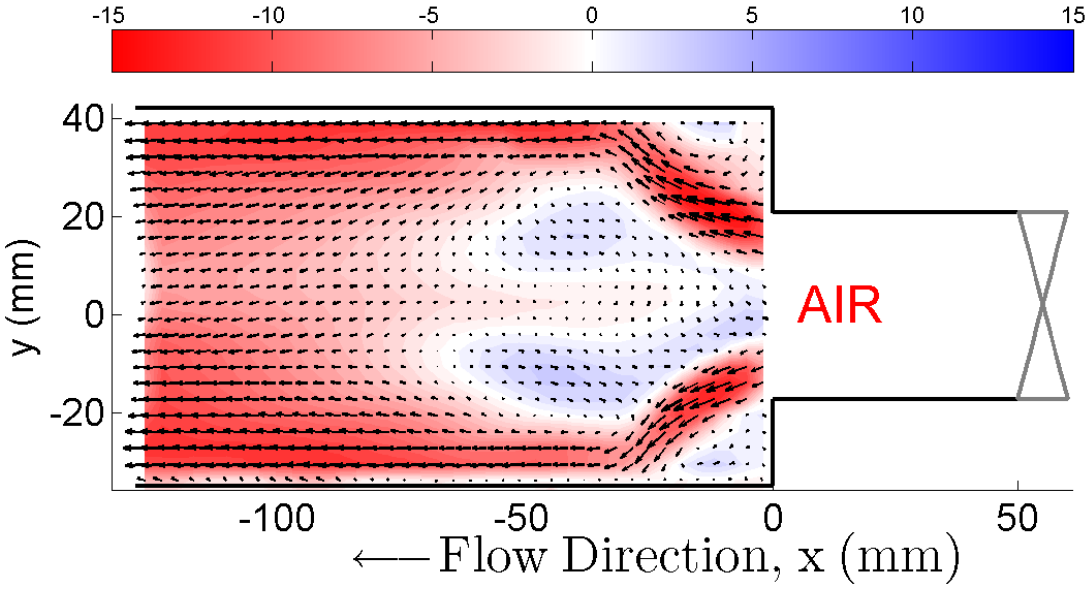

(b) Air at 1960 K

Figure 5-7: Flow field comparisons without a flame in the outer recirculation zone at T_{ad} = 1960 K and Re = 20,000. Colorbar units of x-component velocity are m/s.

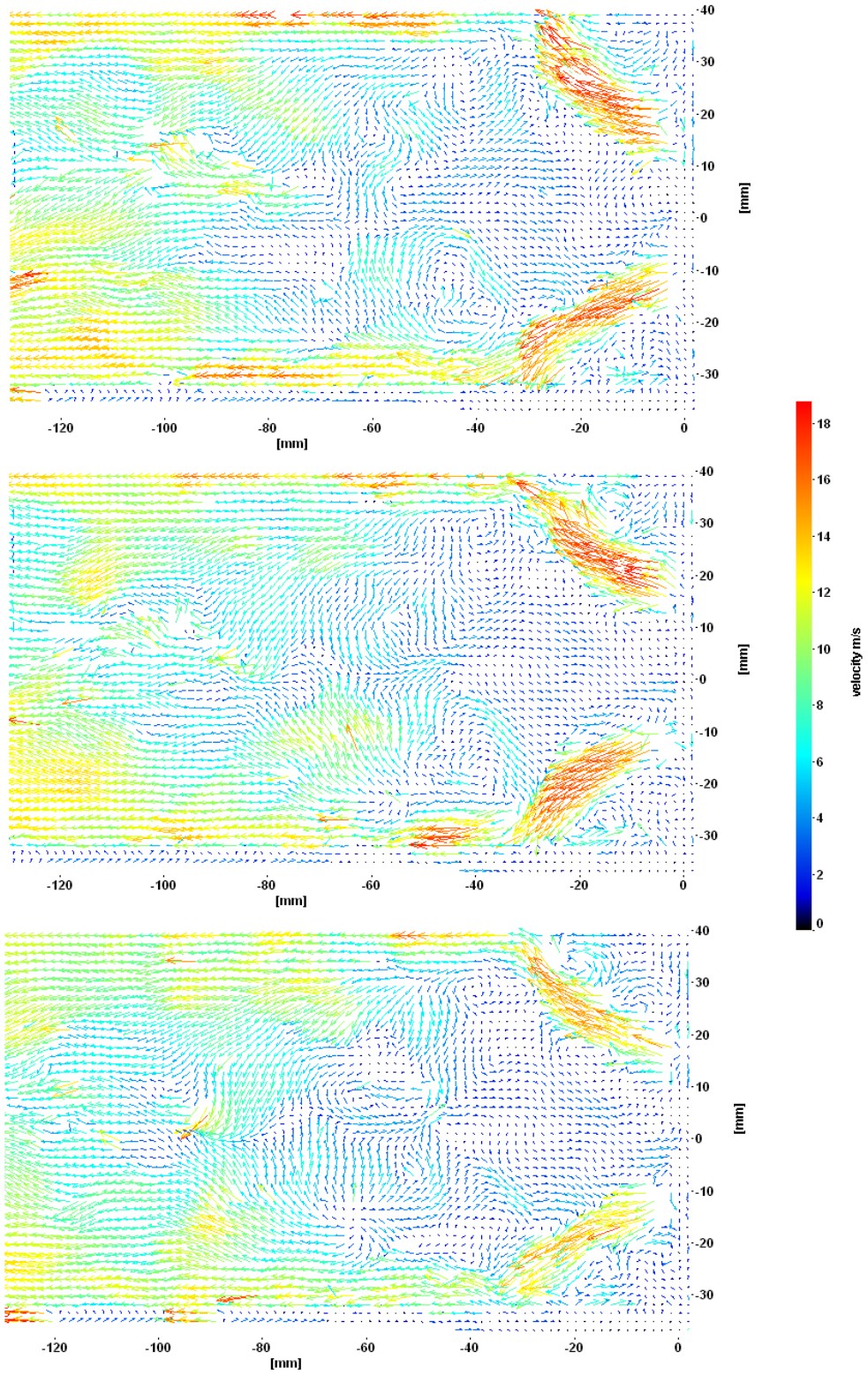

Figure 5-8: Instantaneous PIV Data for air combustion at $\phi = 0.77$ (1960 K). The images, in sequence from top to bottom, are each 1 ms apart.

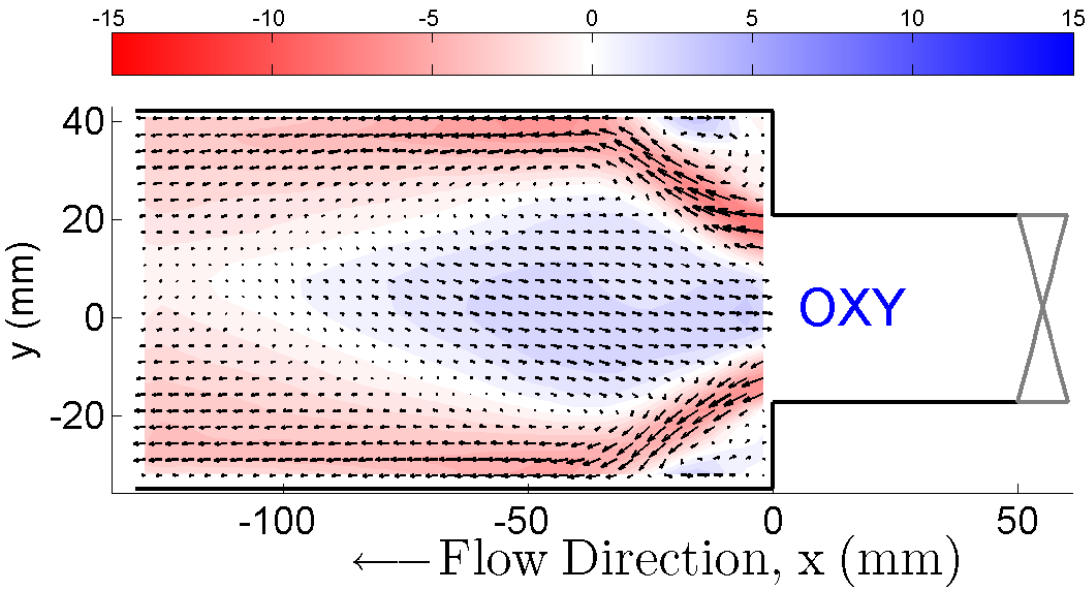

(a) Oxy at 1890 K

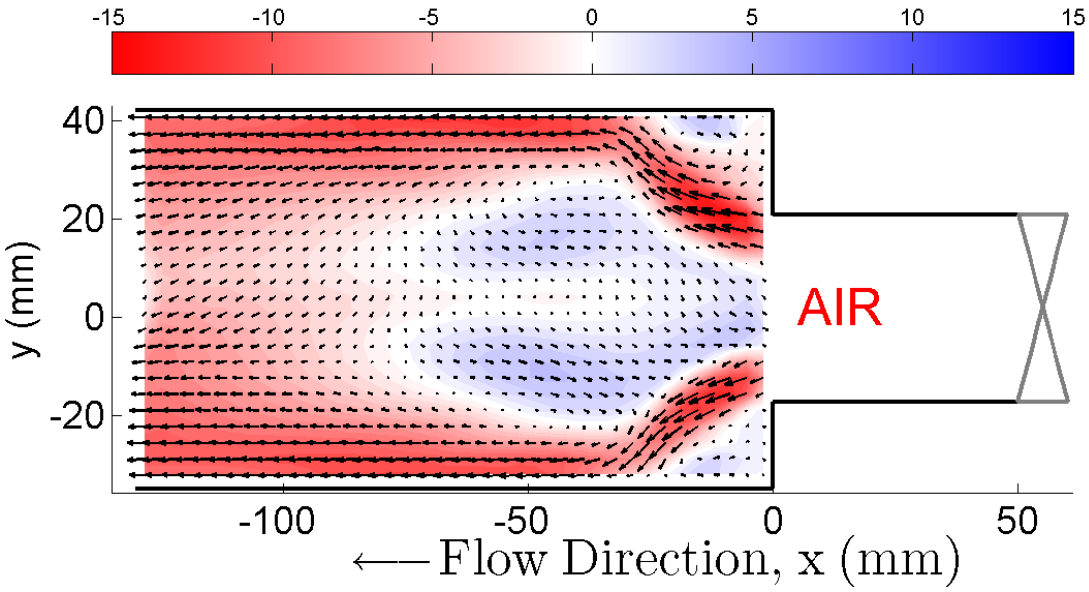

(b) Air at 1890 K

Figure 5-9: Flow field comparisons without a flame in the outer recirculation zone and some degree of waist (for air combustion) at T_{ad} = 1890 K and Re = 20,000. The oxy-combustion case is at the same adiabatic flame temperature but may be in a different mode. Colorbar units of x-component velocity are m/s.

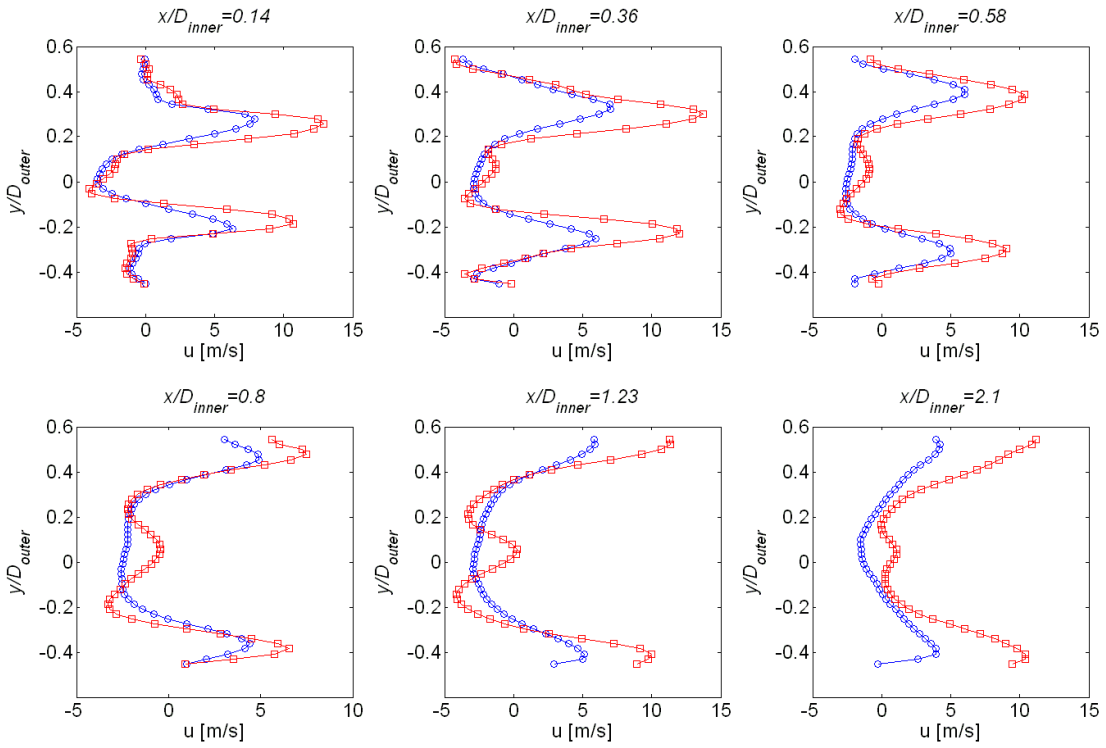

(a) Not normalized

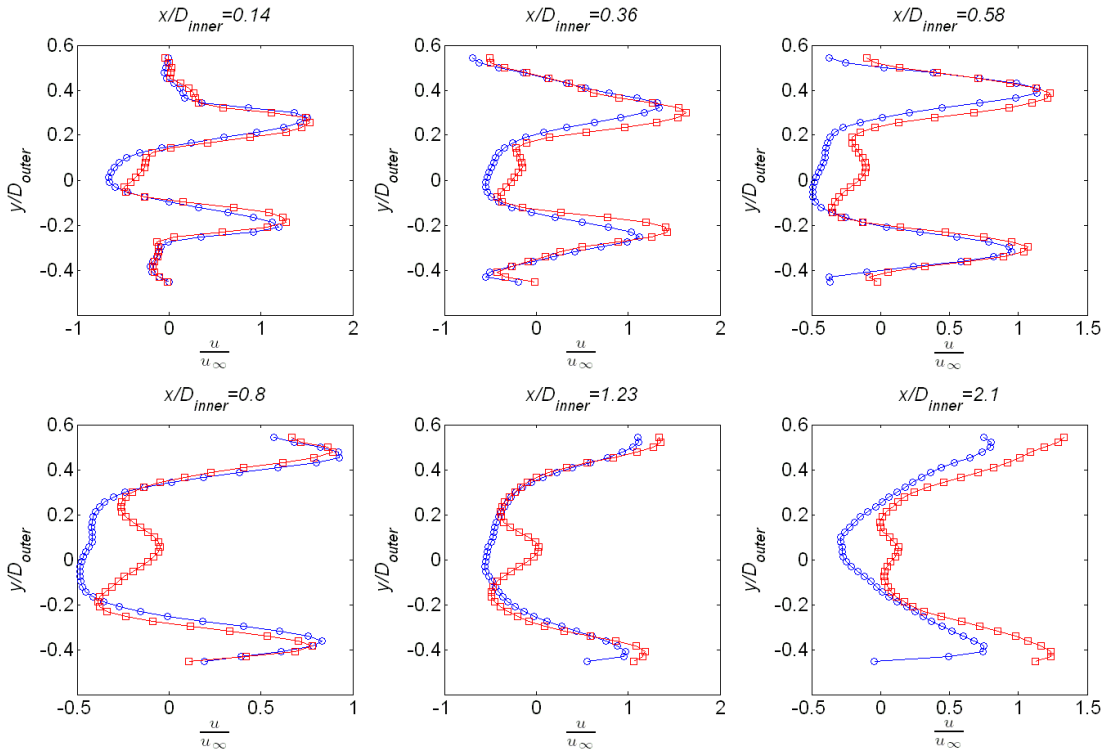

(b) Normalized

Figure 5-10: Velocity profile comparisons at T_{ad} = 1890 K and Re = 20,000. Blue circles are oxy-combustion and red squares are air combustion.

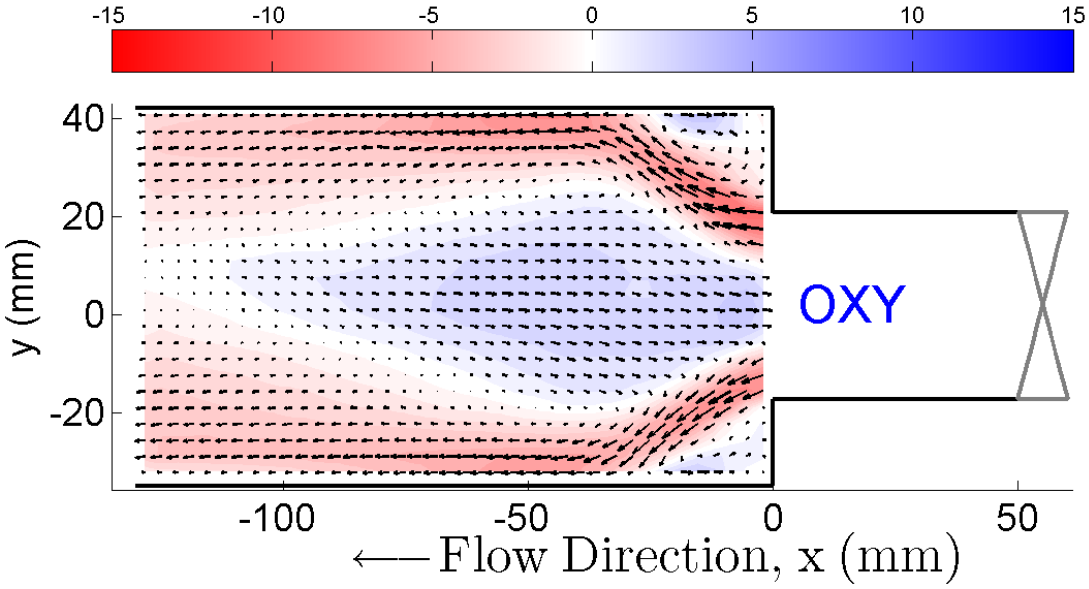

(a) Oxy at 1870 K

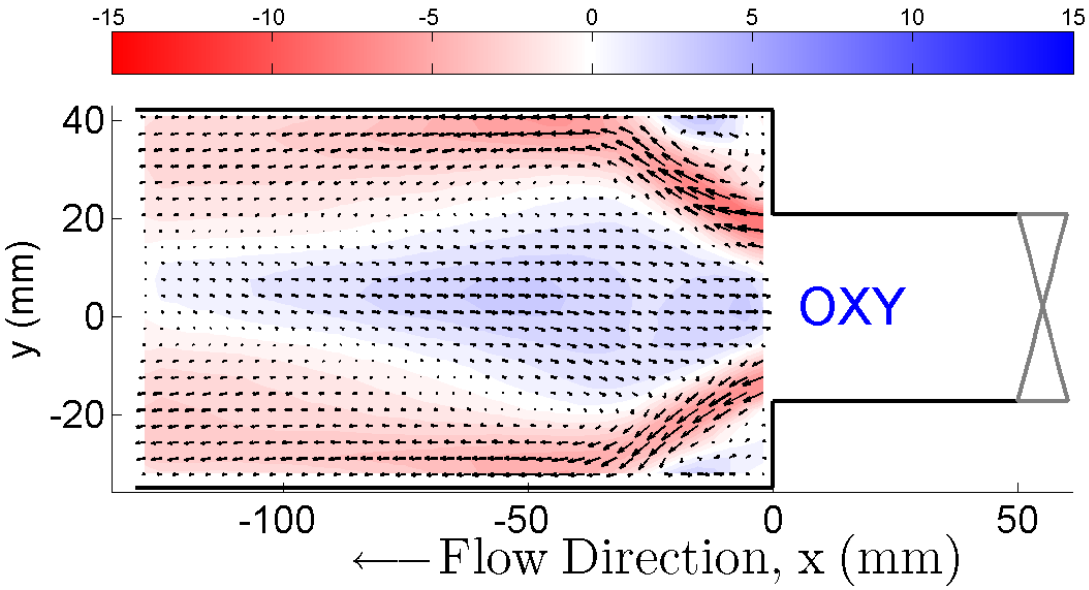

(b) Oxy at 1860 K

Figure 5-11: Flow field comparisons for oxy-combustion at T_{ad} = (a) 1870 K and (b) 1860 K, at Re = 20,000. Colorbar units of x-component velocity are m/s.

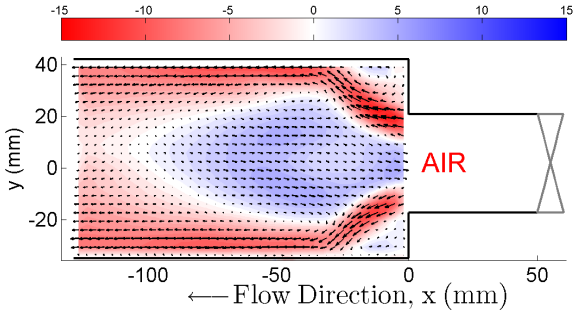

(a) Air at 1850 K

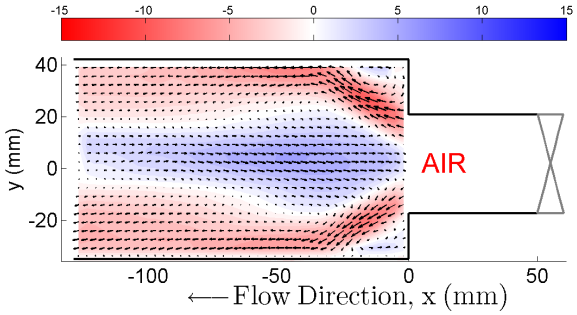

(b) Air at 1830 K

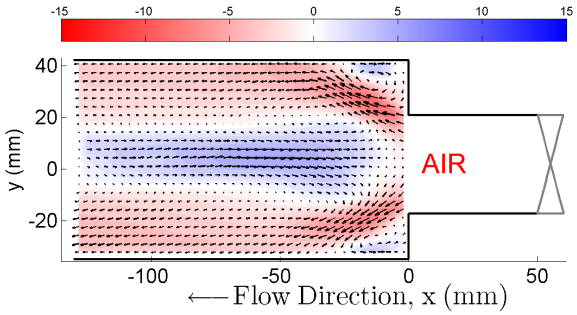

(c) Air at 1810 K

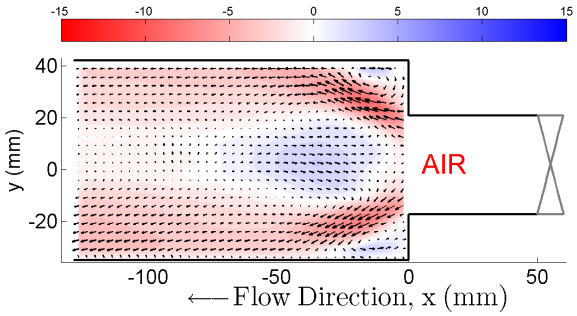

(d) Air at 1790 K

Figure 5-12: Flow field comparisons for air combustion for decreasing T_{ad} at Re = 20,000. Colorbar units of x-component velocity are m/s.

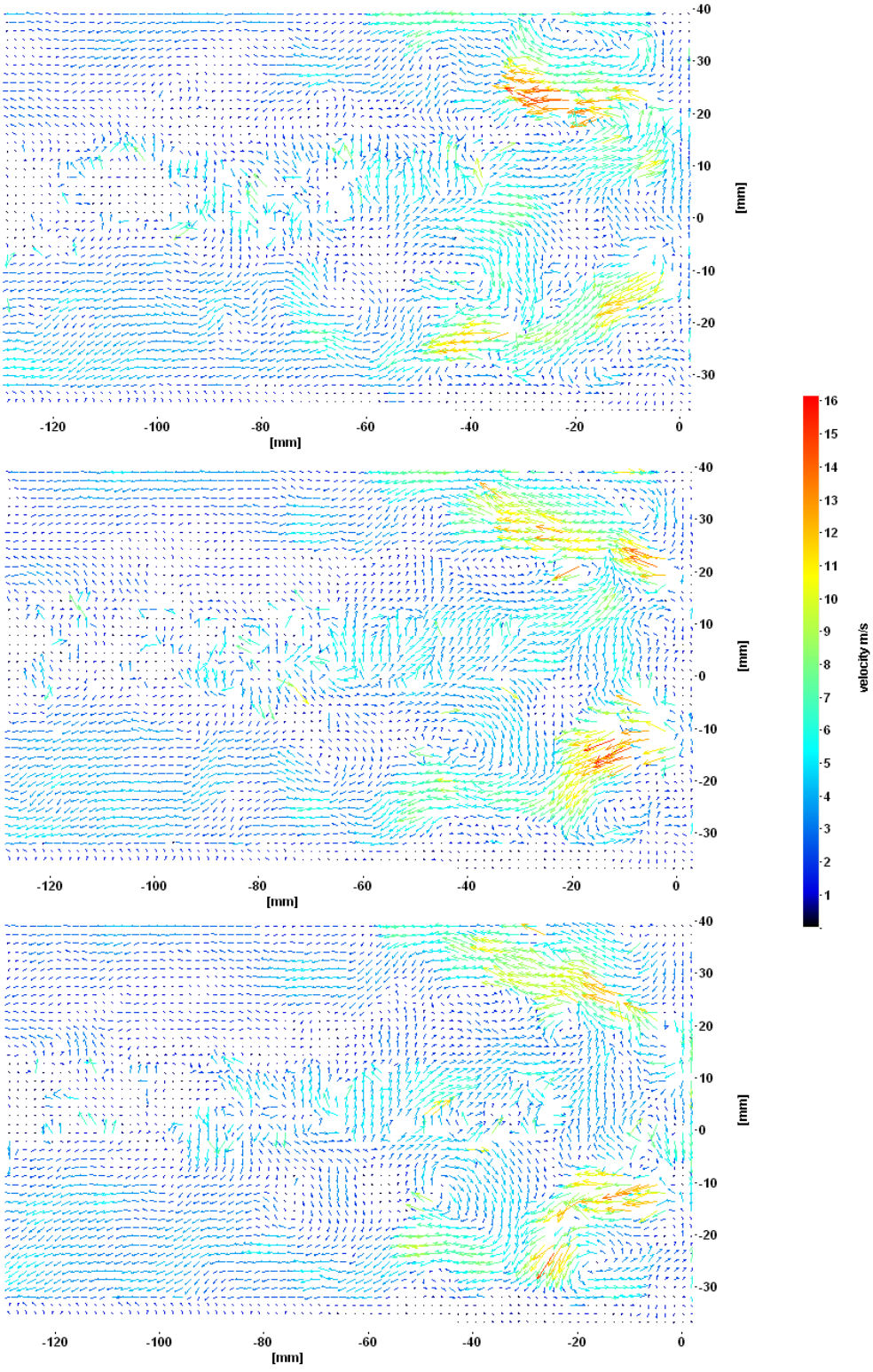

Figure 5-13: Instantaneous PIV Data for air combustion near blowoff at $\phi = 0.67$ (1790 K). The images, in sequence from top to bottom, are each 1 ms apart.

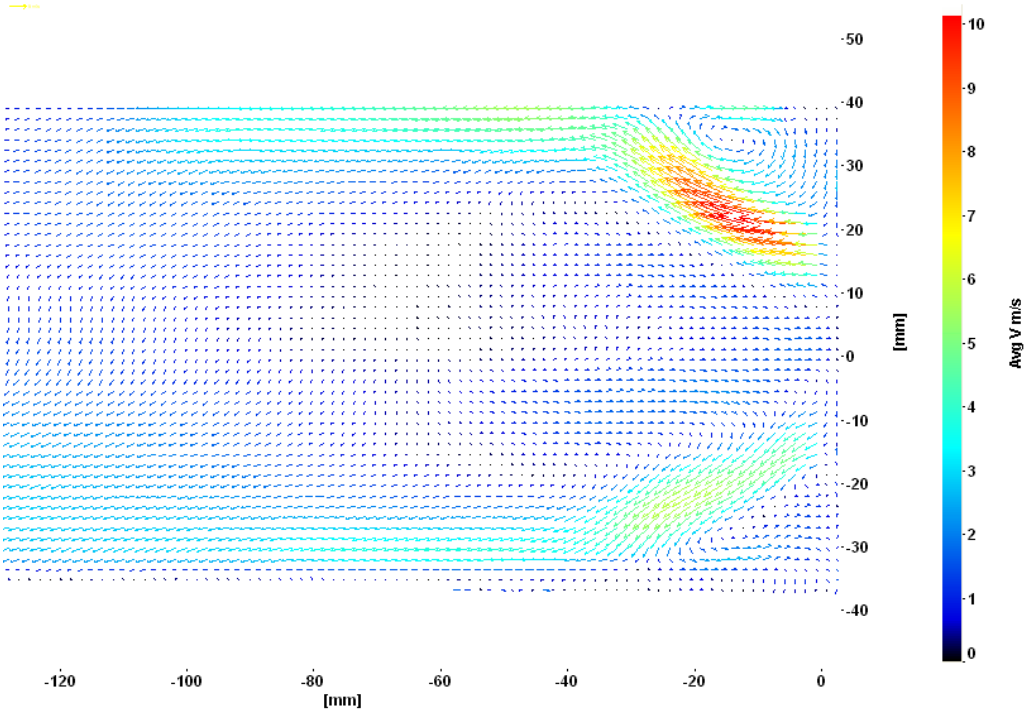

(a) Before adjustment

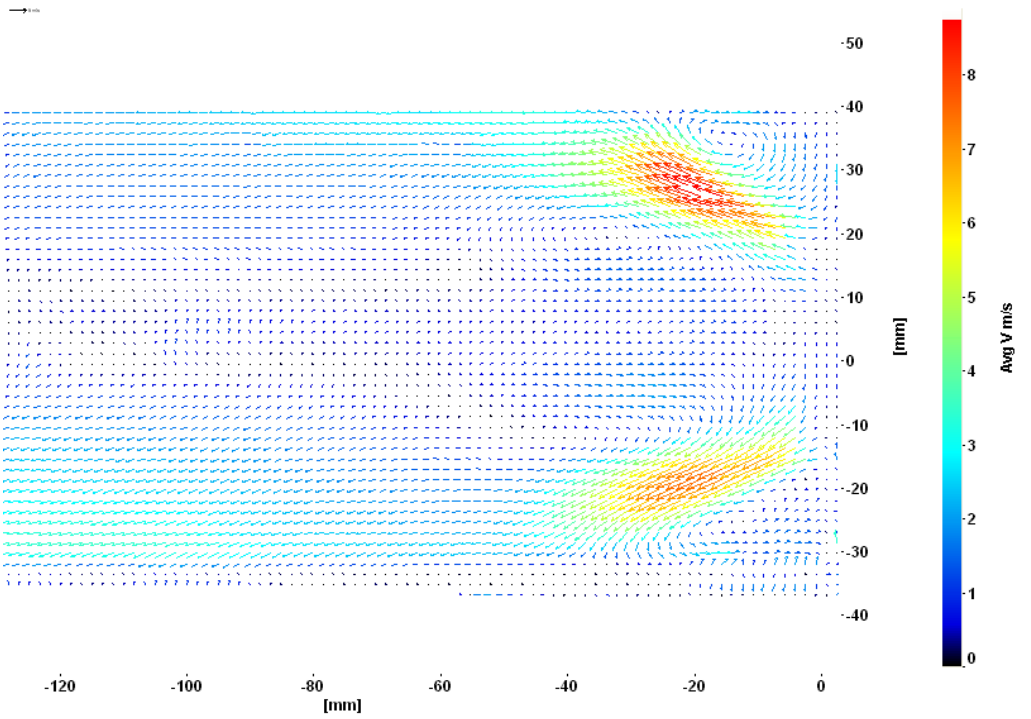

(b) After adjustment

Figure 5-14: Velocity fields from PIV images showing (a) the effect of two igniters protruding into the flow several millimeters at locations 30° from the direction normal to the image and (b) the corrected geometry with recessed igniters. The conditions are cold flow (air) at Re = 20,000.

Chapter 6

Summary and Future Work

6.1 Summary

Oxy-fuel combustion is studied for fundamental flame characteristics in the context of strained flames, combustion instabilities, and blowoff. Developing an understanding of how these fundamentals compare to conventional air combustion is critical in the effective development of new or retrofitted gas turbines for electricity generation.

Comparing near stoichiometric oxy-combustion to air combustion at the same adiabatic flame temperature is a key to contrasting the thermodynamics, transport properties, and chemistry of the reacting mixtures. This substitution of carbon dioxide with the nitrogen in air is shown with a numerical 1-D strained flame to significantly reduce consumption speeds for oxy-combustion due to chemical effects. Competition for the H radical from the presence of carbon dioxide causes high CO emissions, emphasizing the importance of residence time to approach equilibrium in combustor design and the trade-off between carbon monoxide and oxygen emissions.

Experiments on combustion dynamics in an axi-symmetric swirl combustor with premixed flames again show that adiabatic flame temperature is the reaction parameter upon which useful comparisons can be made. Combustion instabilities, upon which much effort is expended to avoid in gas turbines with low pollutant emissions, are described as a baseline for the given combustor geometry using overall sound pressure level maps. These oxy-combustion results are compared to conventional air combus-

tion, finding the collapse of mode transitions with temperature for a given Reynolds number. The ratio of limit cycle frequencies between air and oxy-combustion is explained by the ratio of the speed of sound for the mixtures. Chemiluminescence images of 1/4, 3/4, and 5/4 wave mode limit cycles show similar flame structure and size for air and oxy-combustion even though the theoretical flame areas are much larger for oxy-combustion. This suggests that turbulent mixing plays a key role in the combustion process, and perhaps a different flame model than the strained flame, such as a well-stirred reactor model, could provide better insight into the influence of chemistry and transport. Hysteresis effects in mode transition are important and similar for air and oxy-combustion. This mode history dependence could be used as a strategy in gas turbine operation to avoid combustion instabilities.

Blowoff trends are also analyzed. While oxy-combustion flames blow off at a higher temperature for a given Reynolds number due to weaker flames, there is an unexpected negative slope in blowoff velocity vs temperature for both air and oxy-combustion. The blowoff data are shown to collapse due to blowoff velocity being inversely proportional to the molar heat capacities of the burned gas mixtures at a given power. In the same open exhaust configuration used for blowoff, air and oxy-combustion are shown to go through the same set of transitions in flame structure from high to low temperature at a fixed Reynolds number. Discreet transitions occur with the disappearance of a flame in the outer recirculation zone and from the tulip-shaped flame to the axi-symmetric bubble mode, and a gradual change takes place from the axi-symmetric bubble to a spiral flame near blowoff. Finally, PIV results show that, especially at higher flame temperatures, the normalized stream-wise velocity profiles at different sections along the axis of the combustor collapse for the two types of combustion, providing a useful data set for the validation of numerical work.

6.2 Suggested Future Work

Questions that arise from this work offer multiple paths for further study. In performing simulations, limited knowledge exists on the validity of chemical kinetic mecha-

nisms for oxy-fuel combustion. A greater understanding of the sensitivity specific species concentrations and temperature profiles could lead to better performing systems with low emissions.

Emissions measurements of CO and other species in the experimental combustor would provide useful insight into the practicality and performance of oxy-fuel combustion. While varying equivalence ratio in air combustion and dilution levels in stoichiometric oxy-combustion was chosen for a practical comparison in this work, comparing nitrogen and carbon dioxide-diluted combustion at the same equivalence ratio and adiabatic flame temperature could make fundamental trends more clear. Amplifying the combustion instability results with these variations could provide the kind of insight that can only come from a comprehensive data set. Additionally, much more data analysis should be performed to identify physics that drive the flame characteristics. Coupled with this goal of understanding is the need for models to explain the phenomena and both the similarities and distinctions between air and oxy-combustion.

Likewise, additional work on blowoff trends is warranted by the unique but limited results shown here. It remains to be seen what the complete set of effects are from varying the composition (with other diluents such as Argon), dilution level (temperature), a wider range of Reynolds numbers (turbulence levels), equivalence ratio, fuel type, and fuel mixing (namely with hydrogen). A point of interest is whether there is a critical temperature corresponding to the slope of the blowoff curve on a plot of blowoff velocity vs power. Equipment planned to be put into service includes a planar laser induced fluorescence (PLIF) system. The ultimate goal with this system is to study local flow fields and flame structure with simultaneous PLIF and PIV. Results from PLIF and PIV together near blowoff would be extremely useful in determining the mechanism by which blowoff occurs.

Bibliography

[1] H.M. Altay, R.L. Speth, D.E. Hudgins, and A.F. Ghoniem. Flame-vortex interaction driven combustion dynamics in a backward-facing step combustor. *Combustion and Flame*, 156:1111–25, 2009.

[2] A. Amato, B. Hudak, P. D'Carlo, D. Noble, D. Scarborough, J. Seitzman, and T. Lieuwen. Methane oxycombustion for low CO2 cycles: Blowoff measurements and analysis. *Journal of Engineering for Gas Turbines and Power*, 133, 2011.

[3] A. Amato, B. Hudak, P. D'Souza, P. D'Carlo, D. Noble, D. Scarborough, J. Seitzman, and T. Lieuwen. Measurements and analysis of CO and O2 emissions in CH 4/CO2/O2 flames. volume 33 of *Proceedings of the Combustion Institute*, pages 3399–3405, 2011.

[4] S. Chaudhuri, S. Kostka, M.W. Renfro, and B.M. Cetegen. Blowoff dynamics of bluff body stabilized turbulent premixed flames. *Combustion and Flame*, 157:790–802, 2010.

[5] L. Chen, S. Z. Yong, and A. F. Ghoniem. Oxy-fuel combustion of coal: Characterization, fundamentals, stabilization and CFD modeling.

[6] J. Davison. Performance and costs of power plants with capture and storage of CO2. *Energy*, 32:1163–1176, 2007.

[7] M. Ditaranto and J. Hals. Combustion instabilities in sudden expansion oxy-fuel flames. *Combustion and Flame*, 146:493–512, 2006.

[8] D. Enderton. U.S. electricity fact sheet. Technical report, MIT Energy Club, 2006.

[9] D. Fritsche, M. Furi, and K. Boulouchos. An experimental investigation of thermoacoustic instabilities in a premixed swirl-stabilized flame. *Combustion and Flame*, 151:29–36, 2007.

[10] A. F. Ghoniem. Needs, resources and climate change: Clean and efficient conversion technologies. *Progress in Energy and Combustion Science*, 37:15–51, 2011.

[11] A. F. Ghoniem, A. Annaswamy, W. E. E. Daehyun, Y. I. Tongxun, and S. Park. Shear flow-driven combustion instability: Evidence, simulation, and modeling. In *Twenty-Ninth International Symposium on Combustion Hokkaido University*

Sapporo Japan, July 21, 2002 - July 25, 2002, volume 29, pages 53–60. Combustion Institute, 2002.

[12] A. F. Ghoniem, R. L. Speth, H. M. Altay, and D. E. Hudgins. Dynamics and stability limits of syngas combustion in a swirl-stabilized combustor. In *2008 ASME Turbo Expo, June 9, 2008 - June 13, 2008*, volume 3, pages 767–776, 2008.

[13] P. Glarborg and L. L. B. Bentzen. Chemical effects of a high CO2 concentration in oxy-fuel combustion of methane. *Energy and Fuels*, 22:291–296, 2008. Compendex.

[14] Y. Huang and V. Yang. Dynamics and stability of lean-premixed swirl-stabilized combustion. *Progress in Energy and Combustion Science*, 35:293–364, 2009.

[15] A.J.B. Jackson, H. Audus, and R. Singh. Gas turbine engine configurations for power generation cycles having CO2 sequestration. *Proceedings of the Institution of Mechanical Engineers, Part A (Journal of Power and Energy)*, 218:1–13, 2004.

[16] W. E. Kaskan and A. E. Noreen. High-frequency oscillations of flame held by bluff body. In *American Society of Mechanical Engineers – Meeting A-66, Nov 28-Dec 3 1954*, page 14, 1954.

[17] Peter Kutne, Bhavin K. Kapadia, Wolfgang Meier, and Manfred Aigner. Experimental analysis of the combustion behaviour of oxyfuel flames in a gas turbine model combustor. *Proceedings of the Combustion Institute*, 33:3383–3390, 2011.

[18] H. M. Kvamsdal, K. Jordal, and O. Bolland. A quantitative comparison of gas turbine cycles with CO2 capture. *Energy*, 32:10–24, 2007.

[19] Z. A. LaBry, S. J. Shanbhogue, R. L. Speth, and A. F. Ghoniem. Flow structures in a lean-premixed swirl-stabilized combustor with microjet air injection. volume 33 of *Proceedings of the Combustion Institute*, pages 1575–1581, 2011.

[20] C.K. Law. DYNAMICS OF STRETCHED FLAMES. In *Twenty-Second Symposium (International) on Combustion*, Proceedings of the Combustion Institute, pages 1381–1402, 1988.

[21] G. N. Li, H. Zhou, and K. F. Cen. Emission characteristics and combustion instabilities in an oxy-fuel swirl-stabilized combustor. *Journal of Zhejiang University: Science A*, 9:1582–1589, 2008.

[22] T. C. Lieuwen and V. Yang (ed.). Combustion instabilities in gas-turbine engines. *Progess in Aeronautics and Astronautics*, 210, 2005. ISBN 1-56347-669-X.

[23] T. C. Lieuwen and B. T. Zinn. Experimental investigation of limit cycle oscillations in an unstable gas turbine combustor. In *Thirty-Eighth AIAA Aerospace Sciences Meeting and Exhibit*, 2000. AIAA-2000-0707.

[24] F. Liu, H. Guo, and G. J. Smallwood. The chemical effect of CO2 replacement of n2 in air on the burning velocity of CH4 and h2 premixed flames. *Combustion and Flame*, 133:495–497, 2003.

[25] T. M. Muruganandam and J. M. Seitzman. Characterization of extinction events near blowout in swirl-dump combustors. In *41st AIAA/ASME/SAE/ASEE Joint Propulsion Conference and Exhibit, July 10, 2005 - July 13, 2005*, 41st AIAA/ASME/SAE/ASEE Joint Propulsion Conference and Exhibit, 2005.

[26] S. Nagaraja, K. Kedia, and R. I. Sujith. Characterizing energy growth during combustion instabilities: Singularvalues or eigenvalues? In *32nd International Symposium on Combustion, August 3, 2008 - August 8, 2008*, volume 32 II, pages 2933–2940, 2009.

[27] N. Noiray, D. Durox, T. Schuller, and S. Candel. A unified framework for nonlinear combustion instability analysis based on the flame describing function. *Journal of Fluid Mechanics*, 615:139–167, 2008.

[28] G.A. Richards, K.H. Casleton, and B.T. Chorpening. CO2and H2O diluted oxyfuel combustion for zero-emission power. In *First International Conference on Industrial Gas Turbine Technologies, 10-11 July 2003*, volume 219 of *Proc. Inst. Mech. Eng. A, J. Power Energy (UK)*, pages 121–6, 2005.

[29] S. J. Shanbhogue, S. Husain, and T. Lieuwen. Lean blowoff of bluff body stabilized flames: Scaling and dynamics. *Progress in Energy and Combustion Science*, 35:98–120, 2009.

[30] R. L. Speth and A. F. Ghoniem. Using a strained flame model to collapse dynamic mode data in a swirl-stabilized syngas combustor. In *32nd International Symposium on Combustion, August 3, 2008 - August 8, 2008*, volume 32 II, pages 2993–3000, 2009.

[31] R. L. Speth, Y. M. Marzouk, and A. F. Ghoniem. Impact of hydrogen addition on flame response to stretch and curvature. In *43rd Aerospace Sciences Meeting*. AIAA, 2005. AIAA-2005-143.

[32] Y. Tan, M. A. Douglas, and K. V. Thambimuthu. CO2 capture using oxygen enhanced combustion strategies for natural gas power plants. *Fuel*, 81:1007–1016, 2002.

[33] T. C. Williams, C. R. Shaddix, and R. W. Schefer. Effect of syngas composition and CO2-diluted oxygen on performance of a premixed swirl-stabilized combustor. *Combustion Science and Technology*, 180:64–88, 2008.

[34] M.G. Zabetakis. Flammability characteristics of combustible gases and vapors. Technical report, Bureau of Mines, 1965.

[35] Q. Zhang, D. R. Noble, S. J. Shanbhogue, and T. Lieuwen. Impacts of hydrogen addition on near- lean blowout dynamics in a swirling combustor. In *2007 ASME Turbo Expo, May 14, 2007 - May 17, 2007*, volume 2 of *Proceedings of the ASME Turbo Expo*, pages 189–198, 2007.

[36] D. L. Zhu, F. N. Egolfopoulos, and C. K. Law. Experimental and numerical determination of laminar flame speeds of methane/(Ar, N2, CO2)-air mixtures as function of stoichiometry, pressure, and flame temperature. *Symposium (International) on Combustion*, 22:1537–1545, 1989.

[37] E. E. Zukoski. *Flame Stabilization on Bluff Bodies at Low and Intermediate Reynolds Numbers*. PhD thesis, 1954.